

Plate 1 This schematic depicts the transformations that start with an imaging data sequence and end with a statistical parametric map (SPM). An SPM can be regarded as an 'X-ray' of the significance of regional effects. Voxel-based analyses require the data to be in the same anatomical space: this is effected by realigning the data. After realignment, the images are subject to non-linear warping so that they match a spatial model or template that already conforms to a standard anatomical space. After smoothing, the general linear model is employed to estimate the parameters of a temporal model (encoded by a design matrix) and derive the appropriate univariate test statistic at every voxel (see Figure 2.3). The test statistics (usually t - or F -statistics) constitute the SPM. The final stage is to make statistical inferences on the basis of the SPM and random field theory (see Figure 2.4) and characterize the responses observed using the fitted responses or parameter estimates.

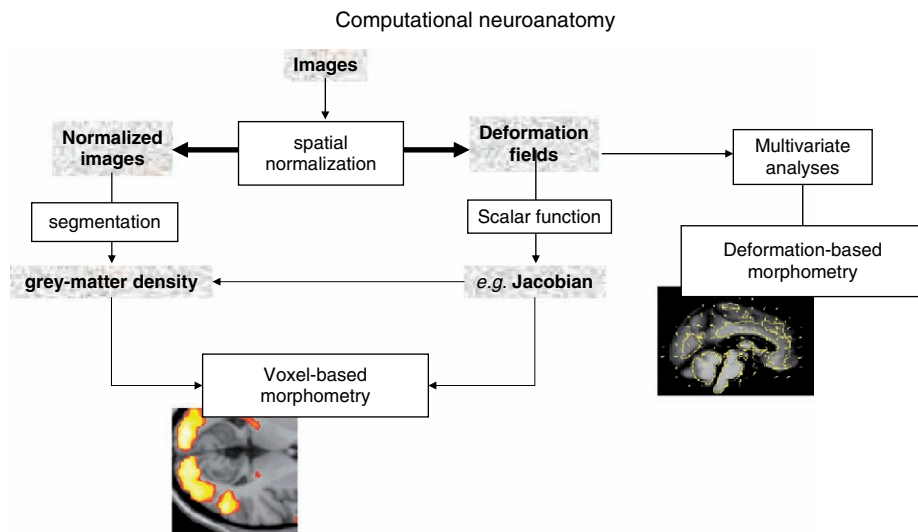


Plate 2 Schematic illustrating different procedures in computational anatomy. After spatial normalization, one has access to the normalized image and the deformation field implementing the normalization. The deformation or tensor field can be analysed directly (deformation-based morphometry) or can be used to derive maps of formal attributes (e.g. compression, dilatation, shear, etc.). These maps can then be subject to conventional voxel-based analyses (tensor-based morphometry). Alternatively, the normalized images can be processed (e.g. segmented) to reveal some interesting aspect of anatomy (e.g. the tissue composition) and analysed in a similar way (voxel-based morphometry). Tensor-based morphometry can be absorbed into voxel-based morphometry. For example, before statistical analysis, Jacobian, or voxel-compression maps can be multiplied by grey-matter density maps. This endows volumetric changes, derived from the tensor, with tissue specificity, based on the segmentation.

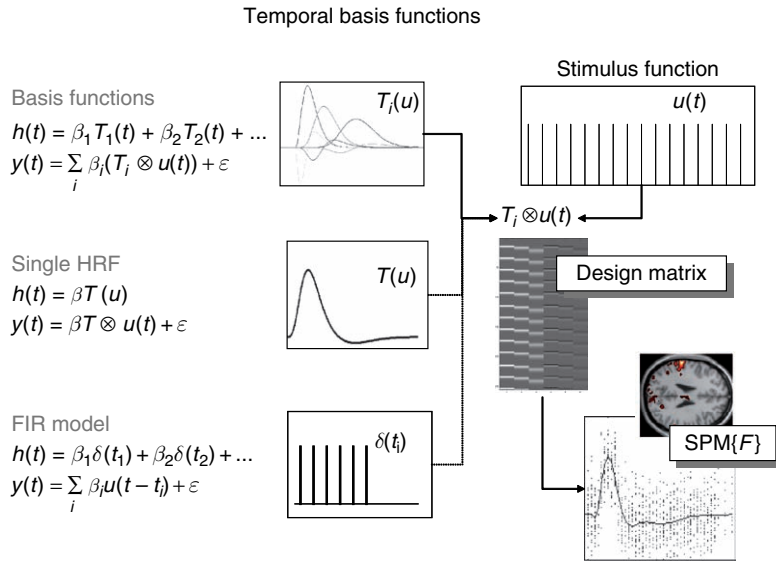


Plate 3 Temporal basis functions offer useful constraints on the form of the estimated response that retain the flexibility of FIR models and the efficiency of single regressor models. The specification of these constrained FIR models involves setting up stimulus functions $u(t)$ that model expected neuronal changes, e.g. boxcar-functions of epoch-related responses or spike-(delta)-functions at the onset of specific events or trials. These stimulus functions are then convolved with a set of basis functions $T_i(t)$ of peristimulus time that, in some linear combination, model the HRF. The ensuing regressors are assembled into the design matrix. The basis functions can be as simple as a single canonical HRF (middle), through to a series of top-hat-functions $\delta_i(t)$ (bottom). The latter case corresponds to an FIR model and the coefficients constitute estimates of the impulse response function at a finite number of discrete sampling times. Selective averaging in event-related fMRI (Buckner *et al.*, 1998) is mathematically equivalent to this limiting case.

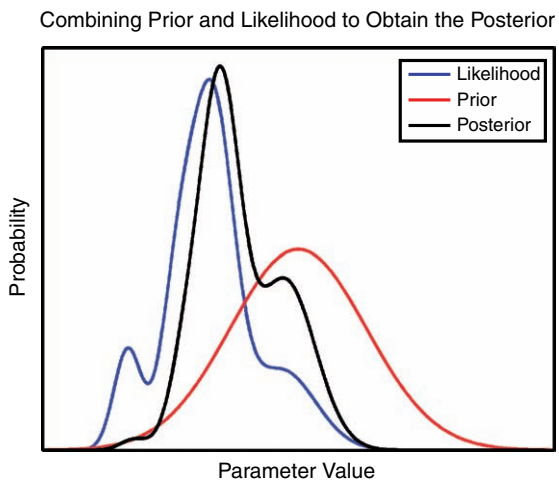


Plate 4 This figure illustrates a hypothetical example of Bayes' theory with a single parameter. By combining the likelihood and prior probability density, it is possible to obtain a tighter posterior probability density. Note that the area under each of the curves is one.

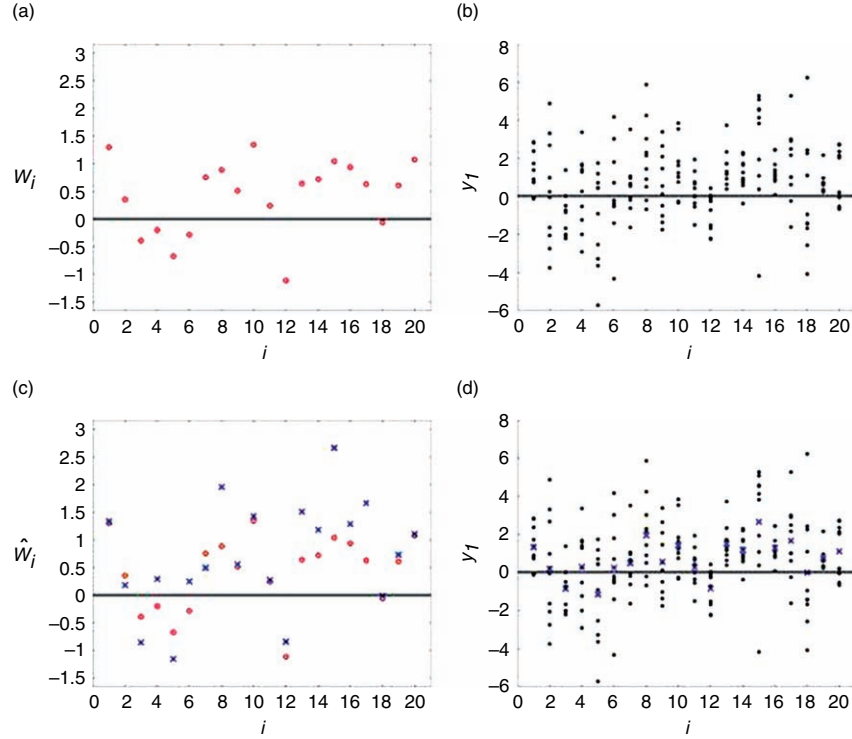


Plate 5 Data for PEB example. (a) Red circles denote ‘true’ effect sizes, w_i , for each voxel i , generated from the prior $p(w_i|\alpha) = N(0, \alpha^{-1})$ with $\alpha = 1$. (b) The black dots denote $n_i = 10$ data points at each voxel generated from the likelihood $p(y_i|w_i) = N(w_i, \beta_i^{-1})$ with β_i drawn from a uniform distribution between 0.1 and 1. Thus some voxels, e.g. voxels 2, 15 and 18, have noisier data than others. Plots (c) and (d) are identical to (a) and (b) but with blue crosses indicating maximum likelihood (ML) estimates of the effect size, \hat{w}_i . These are simply computed as the mean of the data at each voxel, and are used to initialize PEB – see Plate 6.

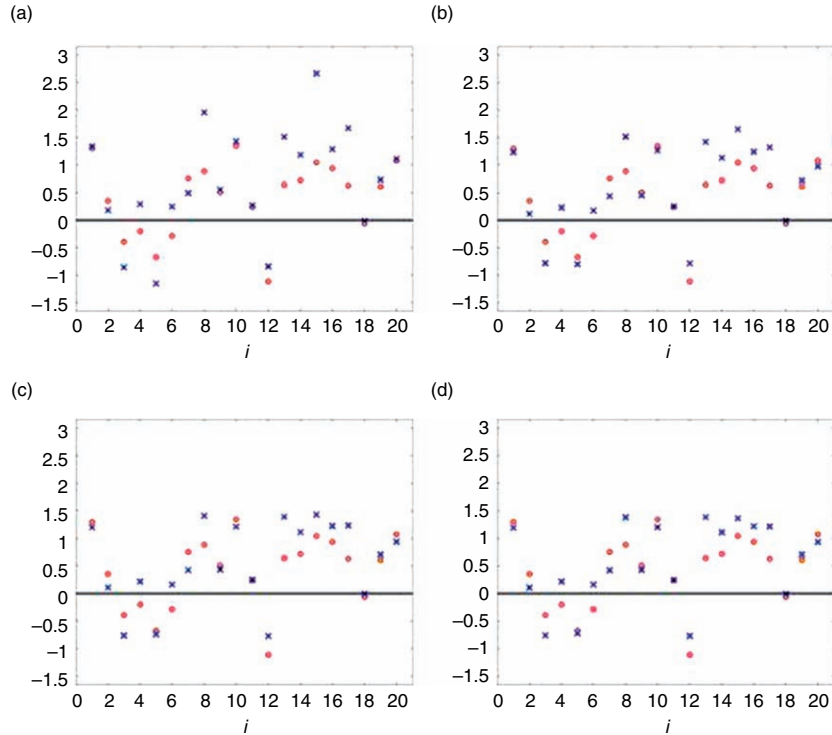


Plate 6 The plots show the true effect sizes, w_i , and estimated effect sizes, \hat{w}_i , before PEB iteration number (a) one, (b) three, (c) five and (d) seven. Plot (a) here is the same as plot (c) in Plate 5, as the estimates were initialized using ML.

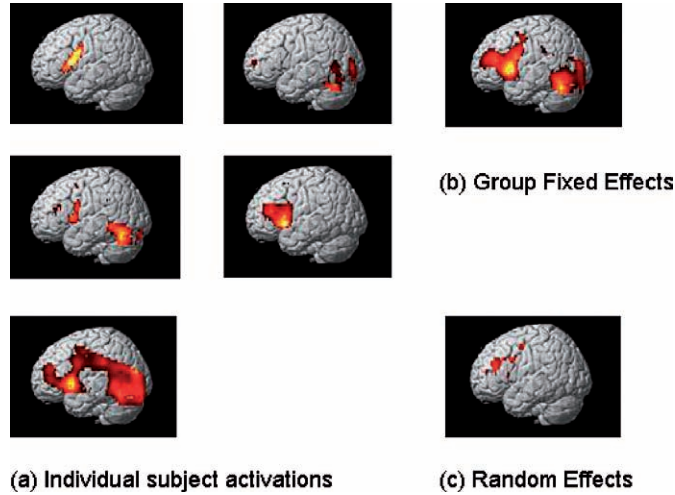


Plate 7 Analysis of PET data showing active voxels ($p < 0.001$ uncorrected). The maps in (a) show the significance of subject-specific effects whereas map (b) shows the significance of the average effect over the group. Map (c) shows the significance of the population effect from an RFX analysis

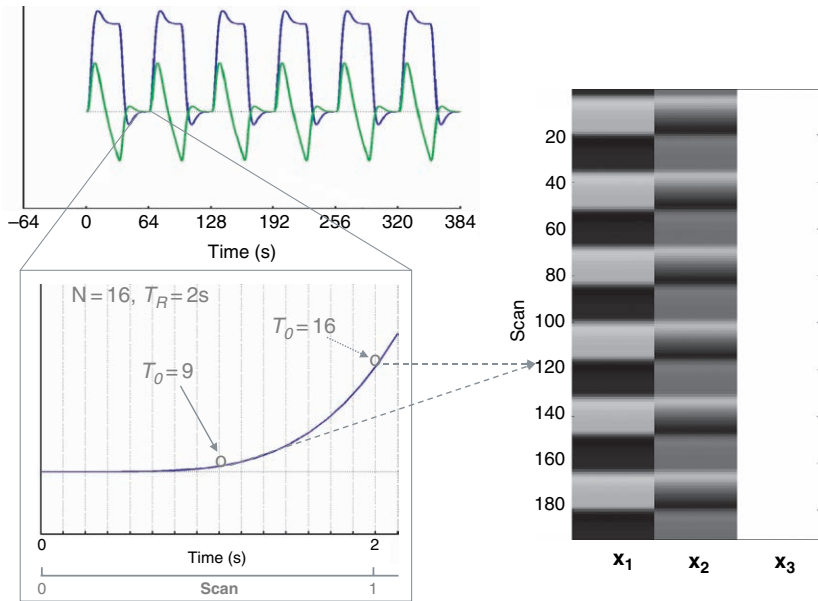


Plate 8 Creation of regressors for design matrix. The predicted BOLD signal for sustained (blue) and decaying (green) activity, during boxcar stimulation after convolution with an HRF in a time-space with resolution $\Delta t = T_R/N$ seconds (upper left). This predicted time course is down-sampled every scan ($T_R = 2\text{s}$) at time point T_0 to create the columns x_1 (boxcar) and x_2 (exponential decay) of the design matrix (together with the constant term x_3). Two possible sample points (T_0) are shown: at the middle and end of the scan (the specific choice should match the relative position of the reference slice within the slice order, if any slice-timing correction is performed).

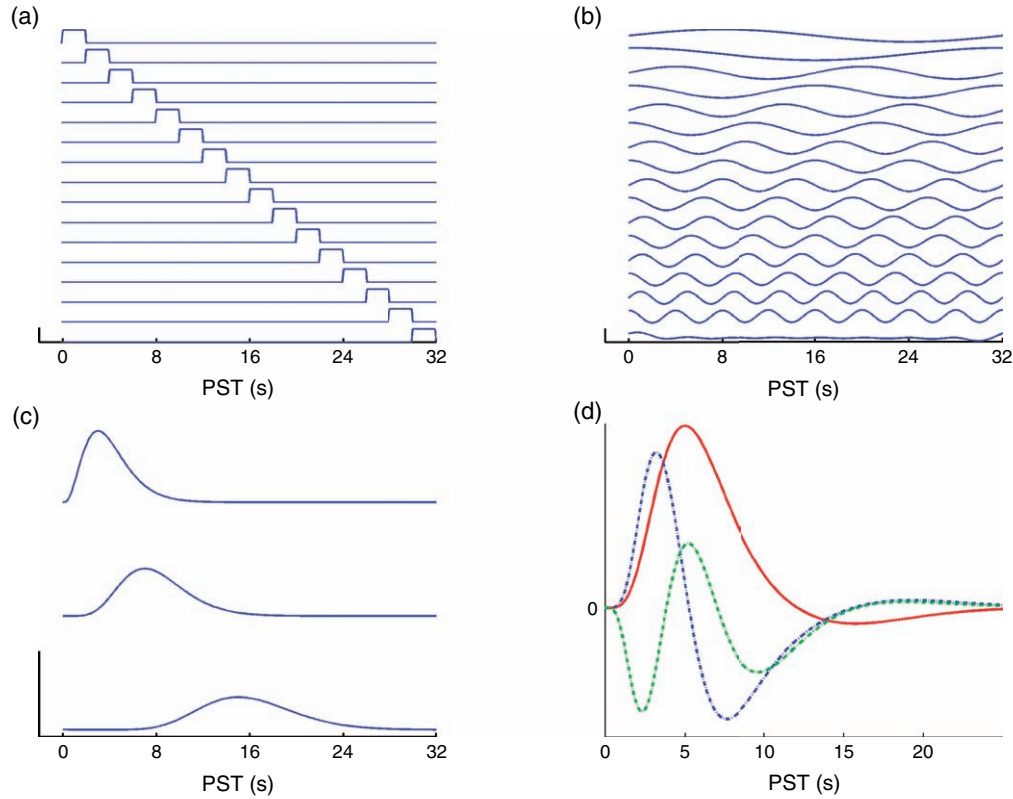
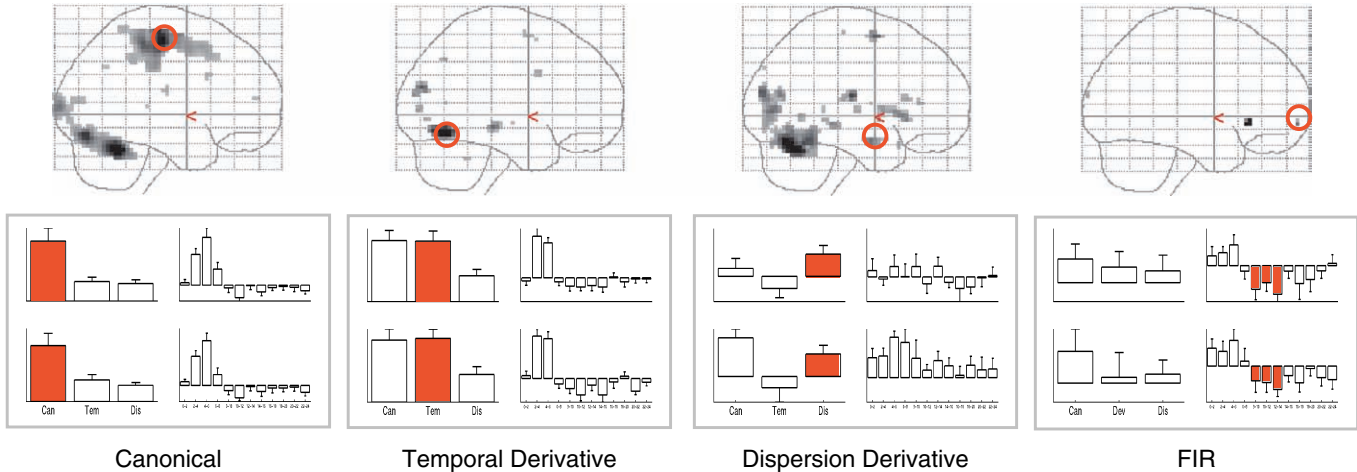


Plate 9 Temporal basis functions offered by SPM, $T = 32\text{s}$: (a) FIR basis set, $K_{FIR} = 16$; (b) Fourier basis set, $K_F = 8$; (c) Gamma functions, $K = 3$; (d) Canonical HRF (red) and its temporal (blue) and dispersion (green) derivatives. The temporal derivative is approximated by the orthogonalized finite difference between canonical HRFs with peak delay of 7 s versus 6 s; the dispersion derivative is approximated by the orthogonalized finite difference between canonical HRFs with peak dispersions of 1 versus 1.01.

(a)



(b)

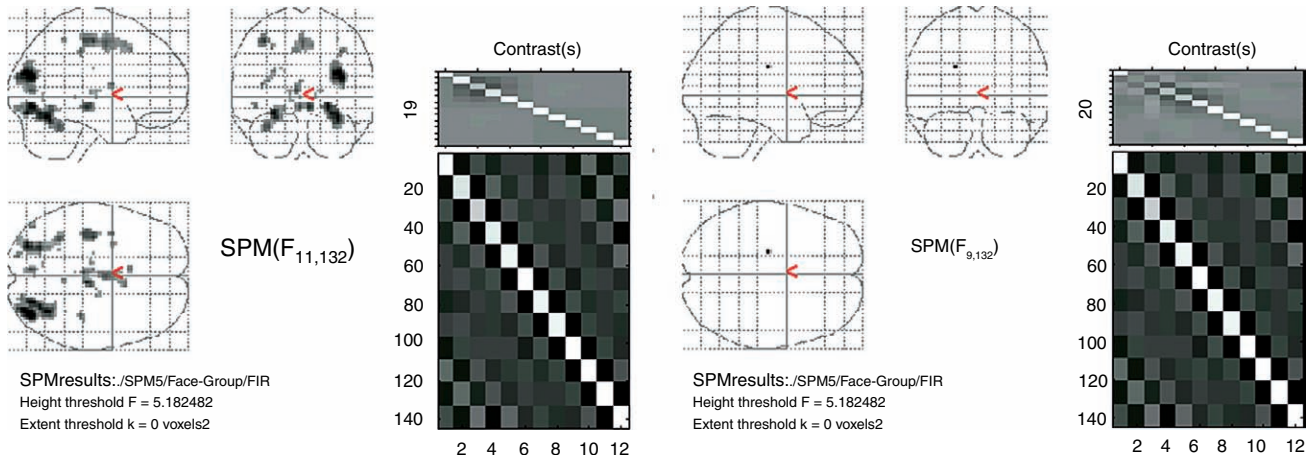


Plate 10 Sufficiency of the informed basis set. In (a), two event-types were modelled with both the informed basis set and an FIR (12 2 s time bins) for 12 subjects within a single, first-level (fixed-effects) design matrix. The event-types were novel or famous faces presented for 0.5 s and requiring a response with the right hand (mean reaction times less than second; see Henson *et al.*, 2002, for more details). The maximum intensity projections (MIP) show F -contrasts thresholded at $p < 0.05$ corrected for (from left to right): the canonical HRF only, its temporal derivative, its dispersion derivative and all time bins of the FIR. The plots below the MIPs show, for the region circled in each MIP, the parameter estimates of the three 'informed' response functions (left) and for a re-fitted FIR (right), for both event-types (upper and low plots). The canonical HRF and its two derivatives explain a lot of variability. A left motor region shows a canonical response (i.e. loading mainly on the canonical HRF); an occipital region shows a response earlier than the canonical; an anterior temporal region shows a response more dispersed than the canonical, but only for the second event-type (famous faces). Little additional variability is, however, picked up by the FIR model: only a few voxels in anterior prefrontal cortex, which show a sustained undershoot (which could reflect a non-haemodynamic artefact). In (b), contrast images of the average of the two event-types for each of 12, 2 s FIR time bins were taken to a second-level ('random effects') analysis. The F -contrast $I - h^+h$, where h is the canonical HRF (sampled every 2 s) and $+$ is the pseudoinverse, shows some regions in which significant variability across subjects is not captured by the canonical HRF (the 'null space' of the canonical HRF; left). The F -contrast $I - H^+H$, on the other hand, where H is now a matrix including the canonical HRF and its two derivatives, shows little that cannot be captured by these three functions (right).

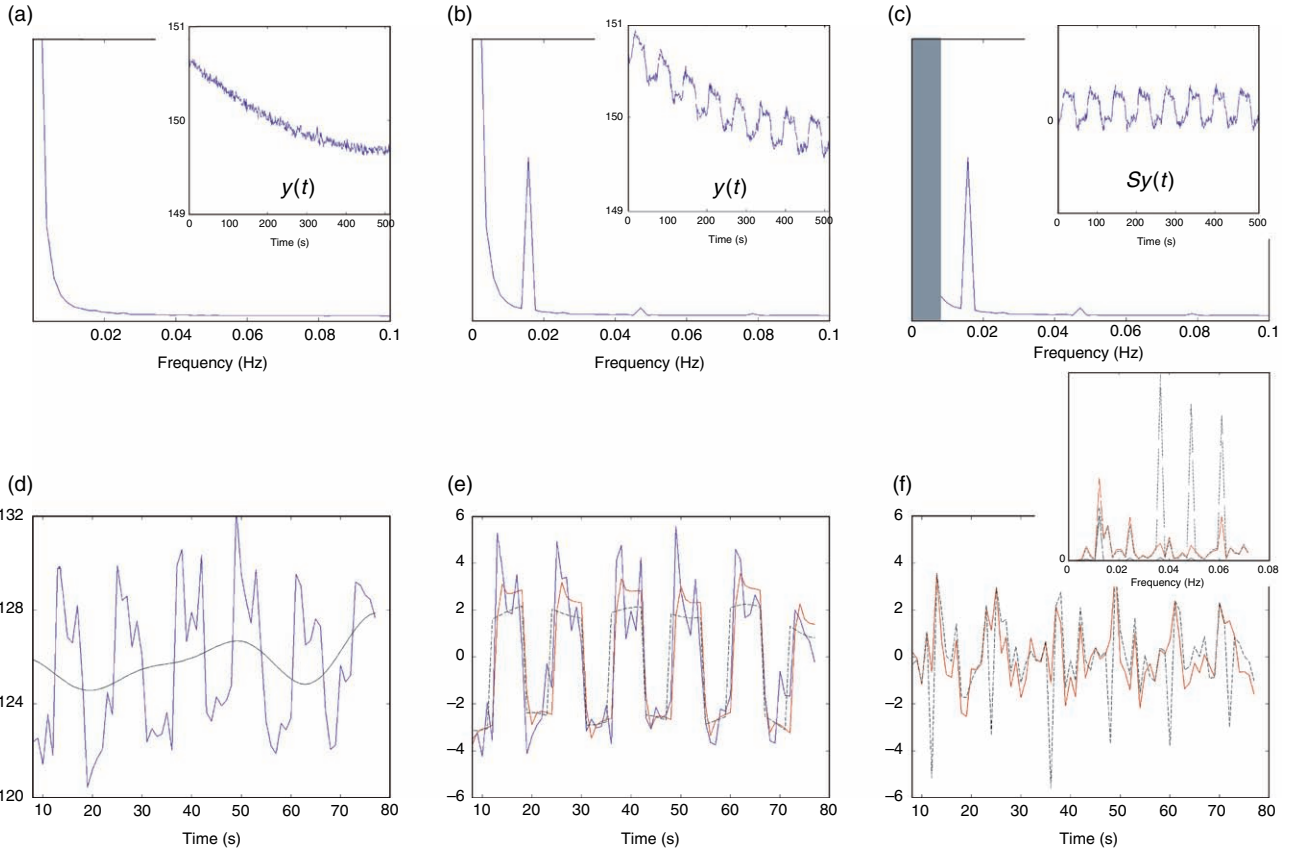


Plate 11 Power spectra, highpass filtering and HRF convolution. Schematic power spectrum and time series (inset) for (a) subject at rest, (b) after square-wave stimulation at 32 s on, 32 s off, (c) after highpass filtering with cut-off 128 s. (d) Real data (blue) and low-frequency drift (black) fitted by DCT highpass filter matrix S (cut-off 168 s) derived from the global maximum in a 42 s on; 42 s off auditory blocked design ($T_R = 7$ s). (e) Fits of a boxcar model with (red) and without (black) convolution by a canonical HRF, together with the data (blue), after application of the highpass filter. (f) Residuals after fits of models with and without HRF convolution: note large systematic errors for model *without* HRF convolution (black) at onset of each block, corresponding to (non-white) harmonics of the stimulation frequency in the residual power spectrum (inset).

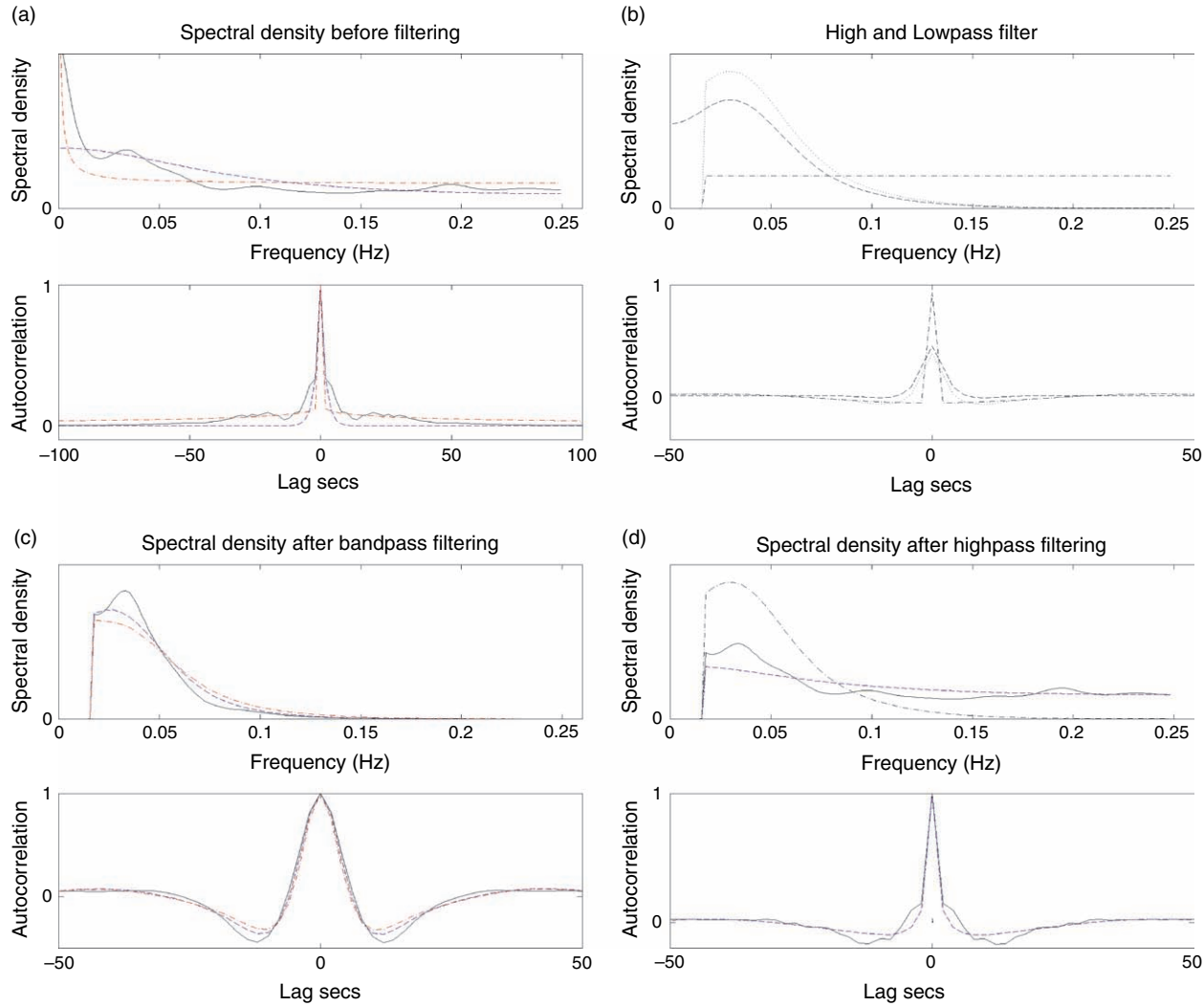


Plate 12 Models of fMRI temporal autocorrelation. Power spectra and autocorrelation functions for: (a) data (solid black), derived from an AR(16) estimation of the mean, globally-normalized residuals from one slice of an event-related dataset; together with fits of an AR(1) model (dashed blue) and 1/f amplitude model (dashed red); (b) high- (dot-dash) and low- (dotted) pass filters, comprising a bandpass filter (dashed); (c) data and both models after bandpass filtering (note that bandpass filter characteristics in (b) would also provide a reasonable approximation to residual autocorrelation); (d) data (solid black) and ReML fit of AR(1)+white noise model (dashed blue) after highpass filtering (also shown is the bandpass filter power spectrum, demonstrating the high-frequency information that would be lost by lowpass smoothing).

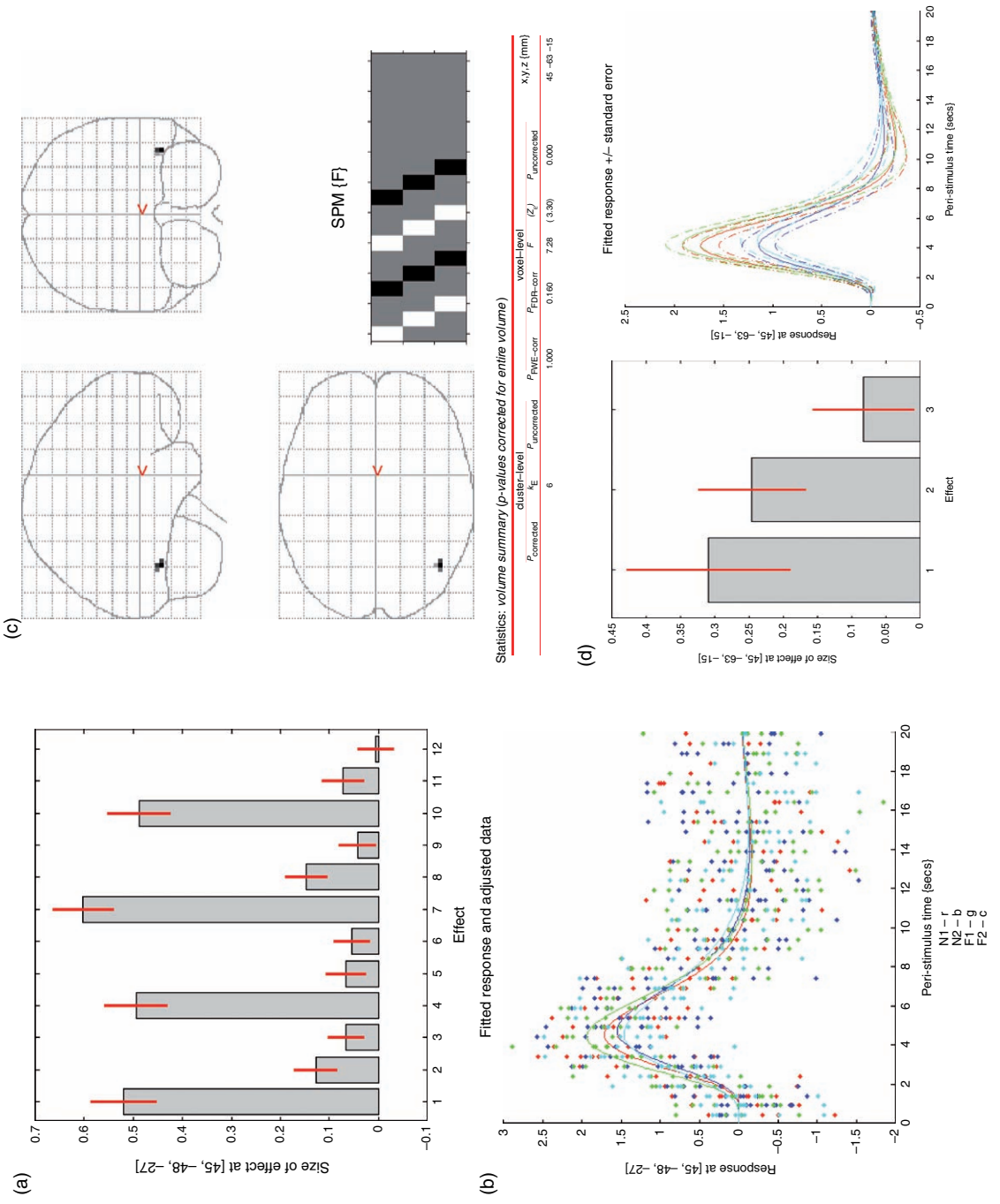


Plate 13 Categorical model: repetition effect. (a) Parameter estimates (scale arbitrary) from local maximum in right fusiform ($+45, -48, -27$), ordered by condition – N1, N2, F1, F2 – and within each condition by basis function – canonical HRF, temporal derivative and dispersion derivative. (b) Fitted event-related responses (solid) and adjusted data (dots) in terms of percentage signal change (relative to grand mean over space and time) against PST for N1 (red), N2 (blue), F1 (green) and F2 (cyan). (c) SPM[F] MIP for repetition effect contrast (inset), thresholded at $p < 0.001$ uncorrected, after inclusive masking with effects of interest (Figure 14.4) at $p < 0.05$ corrected. (d) Contrast of parameter estimates for repetition effect (difference between first and second presentations) in right occipitotemporal region ($+45, -63, -15$) for canonical HRF, temporal derivative and dispersion derivative, together with fitted responses (solid) \pm one standard error (dashed).

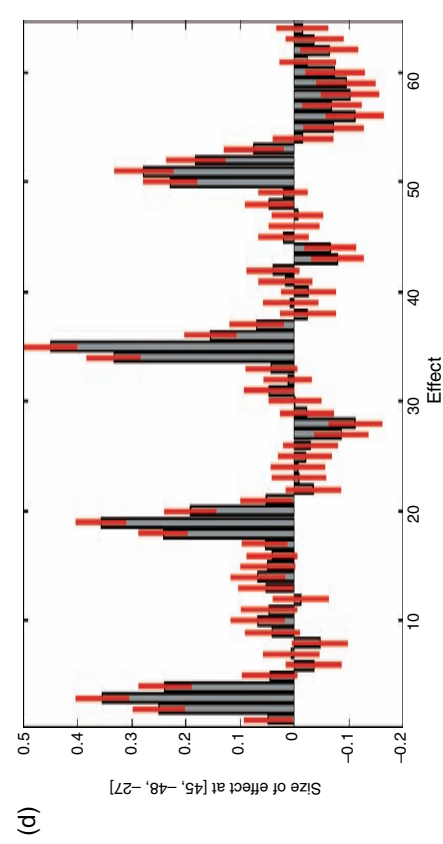
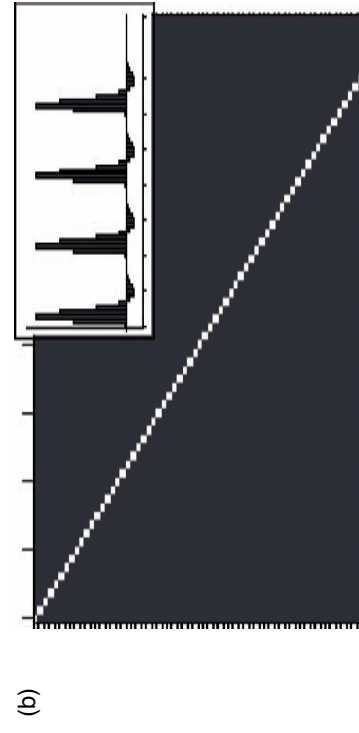
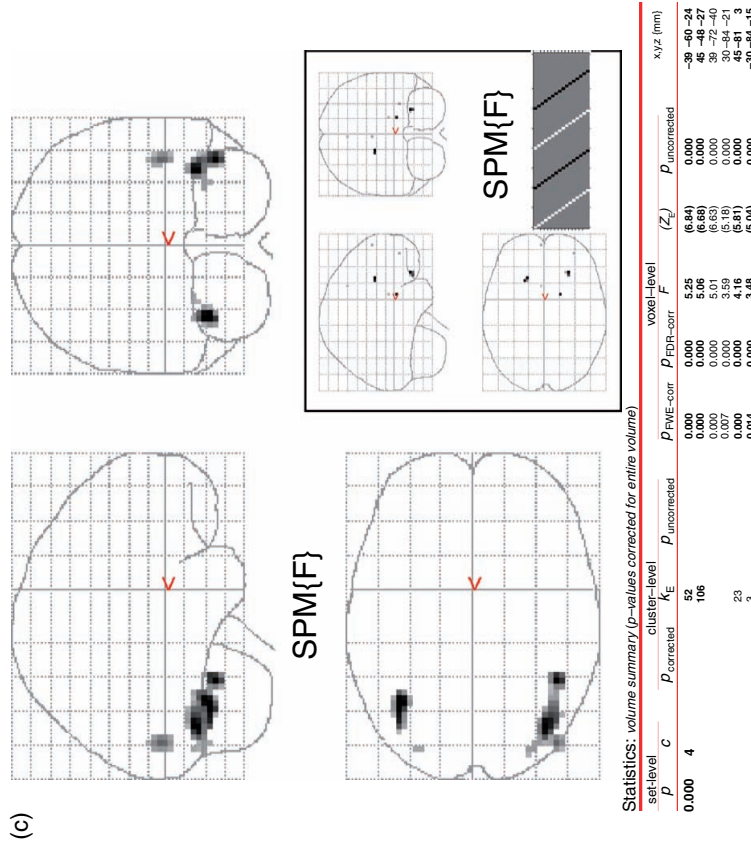
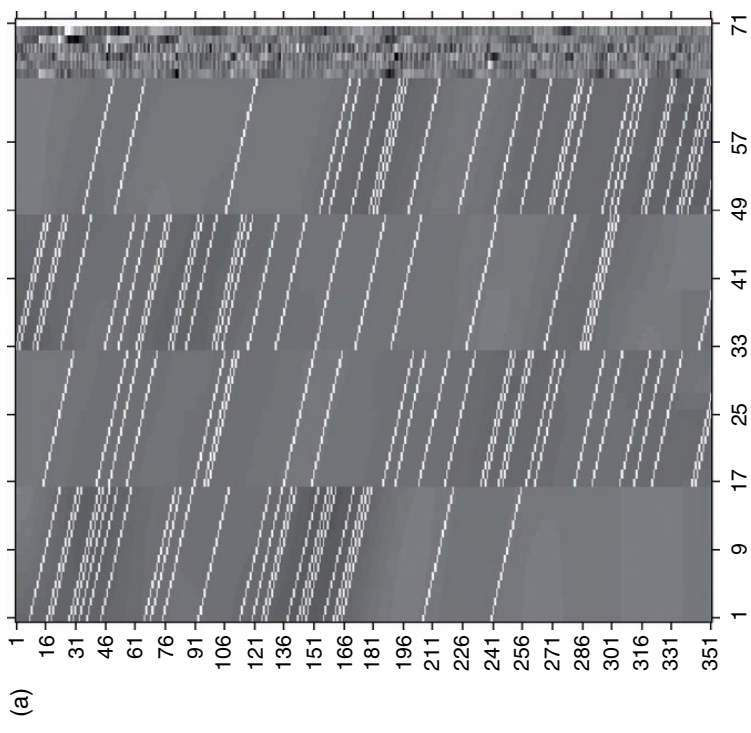


Plate 14 Categorical model: FIR basis set. (a) Design matrix. (b) Effects of interest F -contrast (canonical HRF weighted t -contrast inset). (c) SPM[F] MIP for effects of interest, thresholded at $p < 0.05$ whole-brain corrected, together with SPM tabulated output (inset is SPM[F] for unconstrained repetition effect F -contrast, thresholded at $p < 0.005$ uncorrected). (d) Parameter estimates for effects of interest from right fusiform region ($+45, -48, -27$), as in Plate 13(a), ordered by condition – N1, N2, F1, F2 – and within each condition by the 16 basis functions (i.e. mean response every 2 s from 0 to 32 s PST).

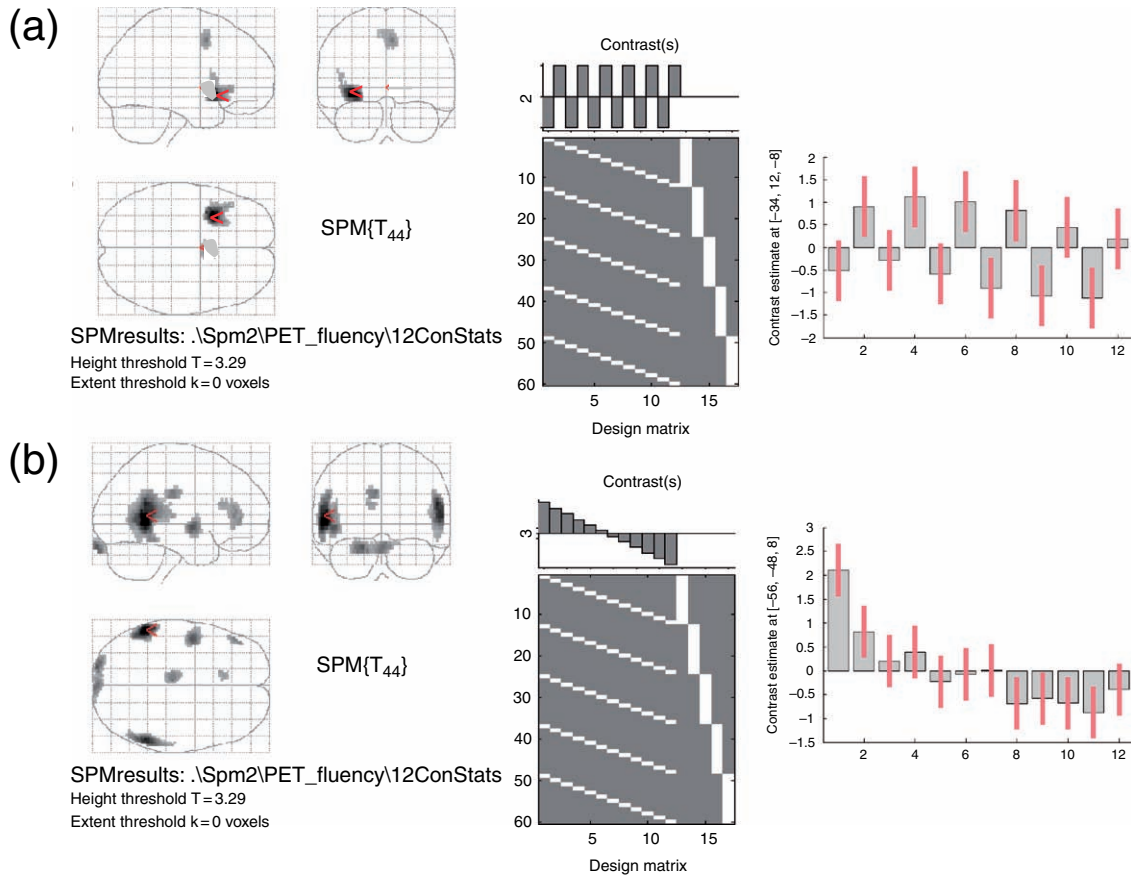


Plate 15 A simple design matrix with 5 subjects (sessions) and 12 conditions. (a) A simple subtraction of two levels of a categorical factor (Generate minus Read) that alternate six times. (b) A linear contrast across a parametric factor, time during experiment, with 12 levels.

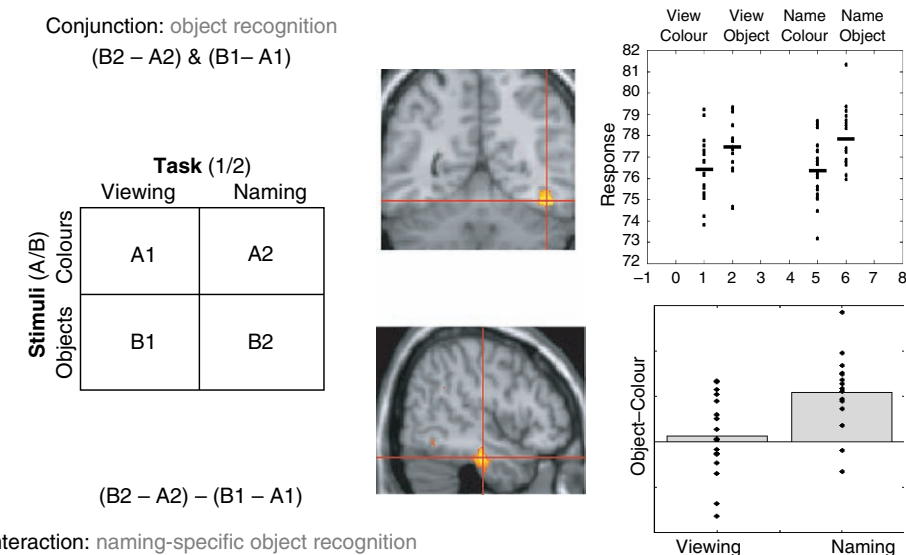


Plate 16 Cognitive conjunction and interactions (from Price and Friston, 1997). (Upper panels) The conjunction of two contrasts shows a posterior temporal region that is activated when an object is present, regardless of whether the task was passive viewing or naming. (Lower panels) When the same conditions are treated as a 2×2 factorial design (left), an interaction contrast reveals a more anterior temporal region that is only active when an object is present and subjects are naming that object.

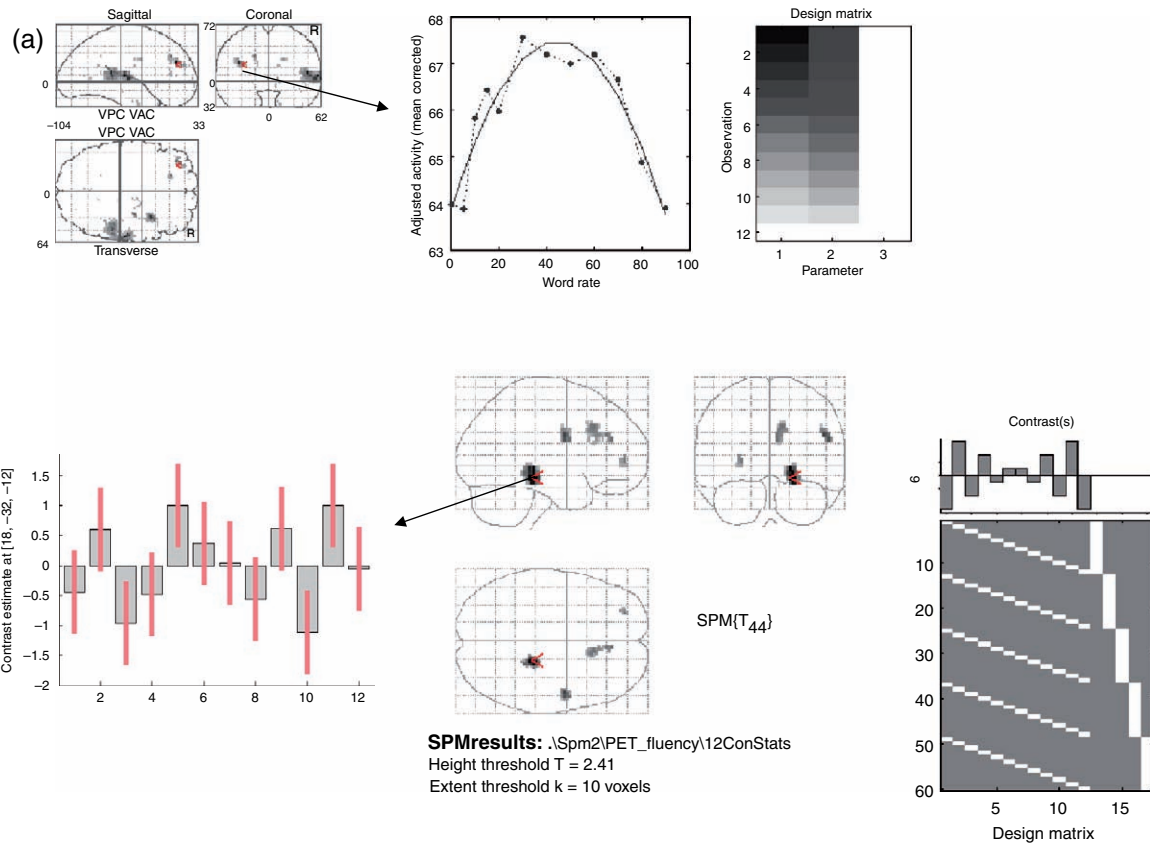


Plate 17 (a) Non-linear effects of a parametric factor modelled in a single-subject design matrix using a second-order polynomial expansion. (b) A linear time-by-condition interaction contrast in a 2×6 factorial design across 5 subjects.

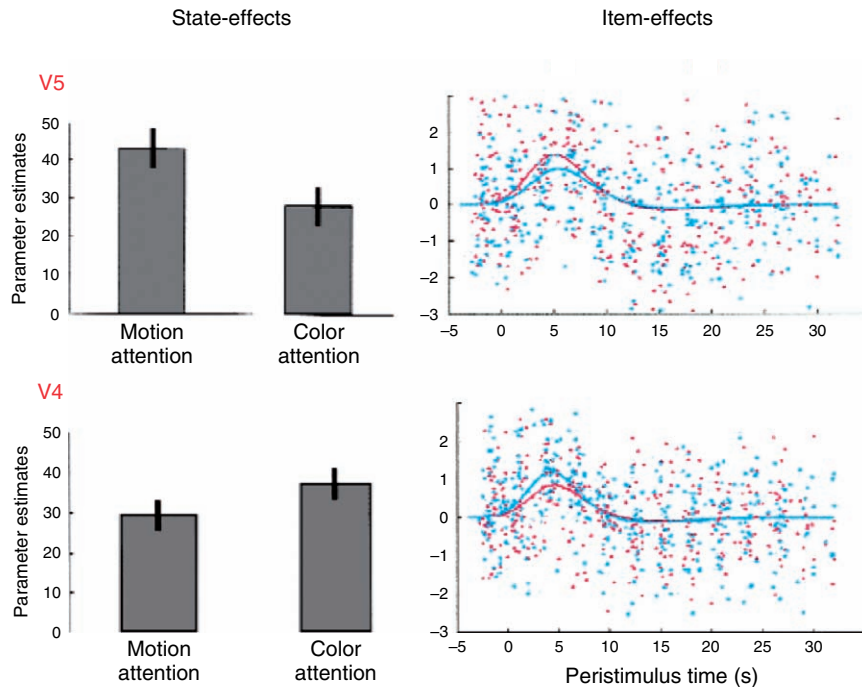


Plate 18 State- and item-effects (from Chawla *et al.*, 1999). Attention to colour of radially-moving coloured dots increased both baseline activity (top left) and evoked responses (top right) – i.e. both offset and gain – in V4 relative to attention to motion. The opposite pattern was found in V5 (bottom row).

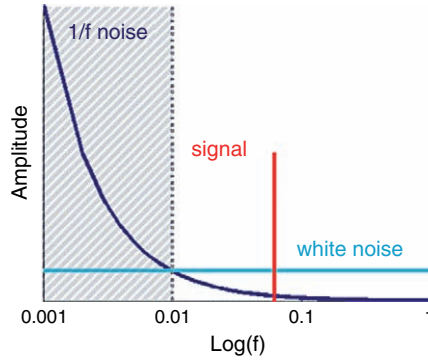


Plate 19 Schematic form of $1/f$ and white noise (dark and light blue respectively) typical of fMRI data, together with experimentally-induced signal at 0.03 Hz (red) and highpass filtering (hatched area).

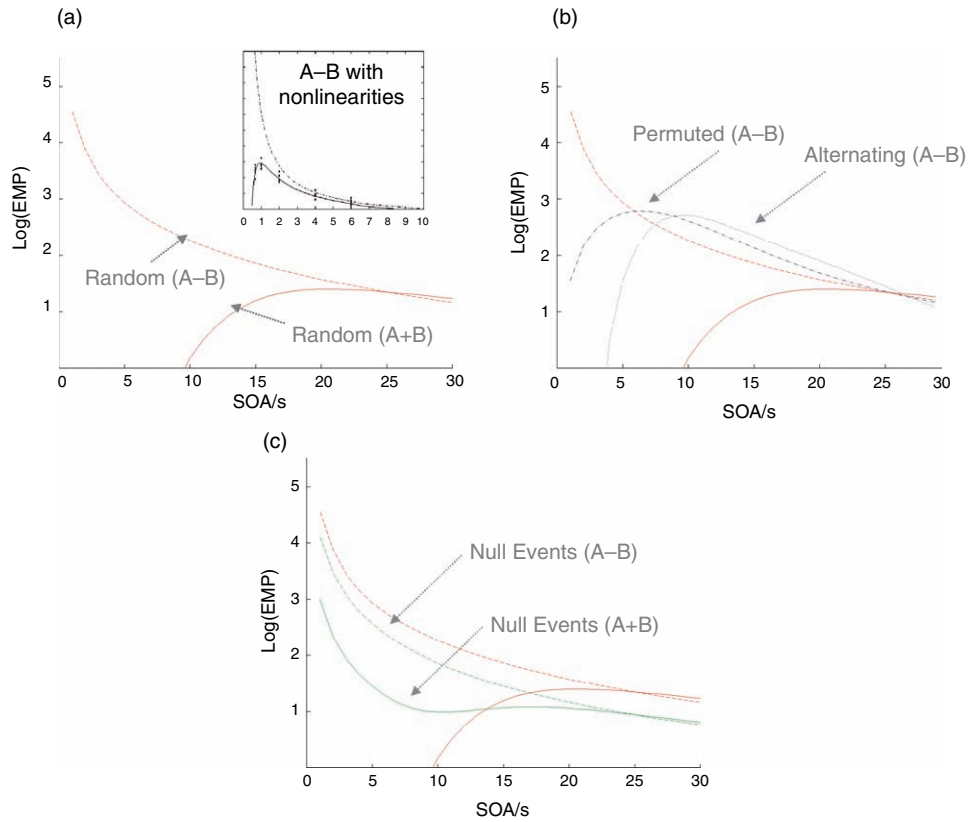


Plate 20 Efficiency for two event-types (from Josephs and Henson, 1999). Efficiency is expressed in terms of ‘estimated measurable power’ (EMP) passed by an effective HRF, characterized by a canonical HRF, highpass filter with cut-off period of 60 s and lowpass smoothing by a Gaussian 4 s full-width at half maximum (FWHM), as a function of Δt for main (solid) effect ($[1 \ 1]$ contrast) and differential (dashed) effect ($[1 \ -1]$ contrast). (a) Randomized design. (b) Alternating (black) and permuted (blue) designs. (c) With (green) and without (red) null events. Insert: effect of non-linearity (saturation) on average response as a function of SOA within a 32 s blocked design. Solid line: average response to a train of stimuli predicted using a second-order Volterra model of haemodynamic responses. The broken line shows the predicted response in the absence of non-linear or second-order effects (Friston *et al.*, 2000).

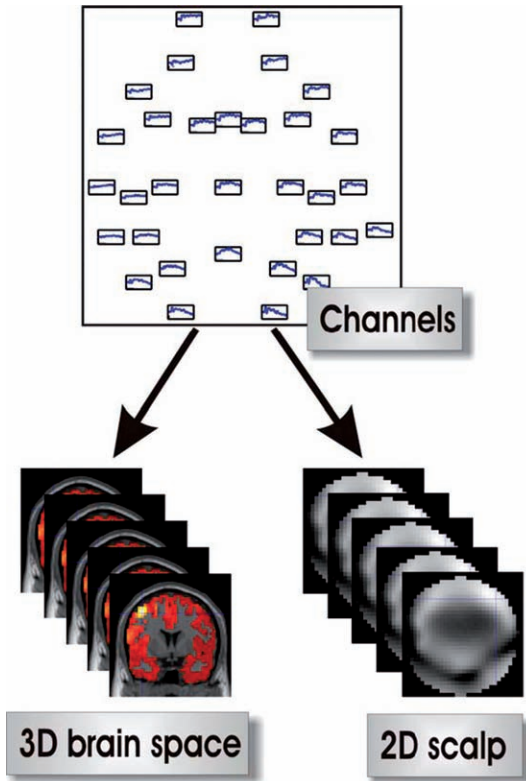


Plate 21 For each trial type and subject, the ERR, for each channel, is projected to either three-dimensional brain space (source reconstruction) or interpolated on the scalp surface. This results in either 3-D or 2-D image time-series.

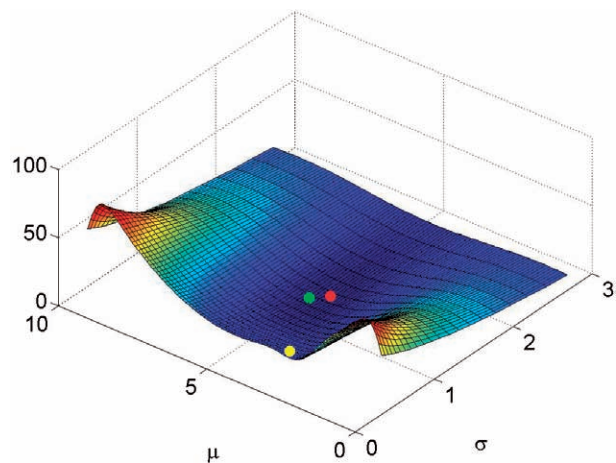


Plate 22 KL-divergence, $KL(q||p)$ for p as defined in Figure 24.2 and q being a Gaussian with mean μ and standard deviation σ . The KL-divergences of the approximations in Figure 24.2 are (a) 11.73 for the first mode (yellow ball), (b) 0.93 for the second mode (green ball) and (c) 0.71 for the moment-matched solution (red ball).

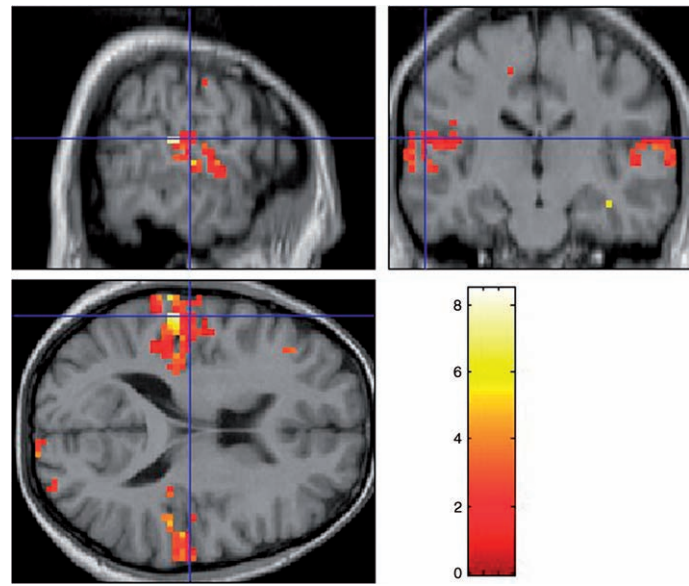


Plate 23 PPM for positive auditory activation. Overlay of effect-size, in units of percentage of global mean, on subjects' MRI for above-threshold voxels. The default thresholds were used, i.e., we plot c_n for voxels which satisfy $p(c_n > 0) > 1 - 1/N$.

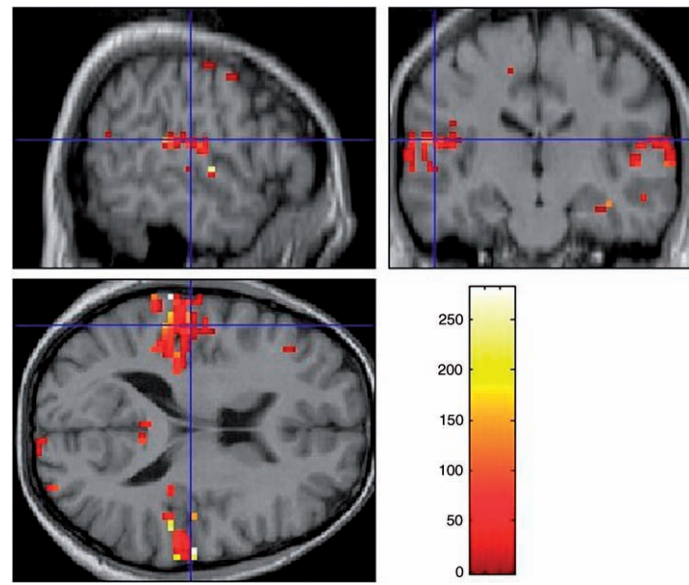


Plate 24 PPM for positive or negative auditory activation. Overlay of χ^2 statistic on subjects' MRI for above-threshold voxels. The default thresholds were used, that is, we plot χ_n^2 for voxels which satisfy $p(c_n > 0) > 1 - 1/N$.

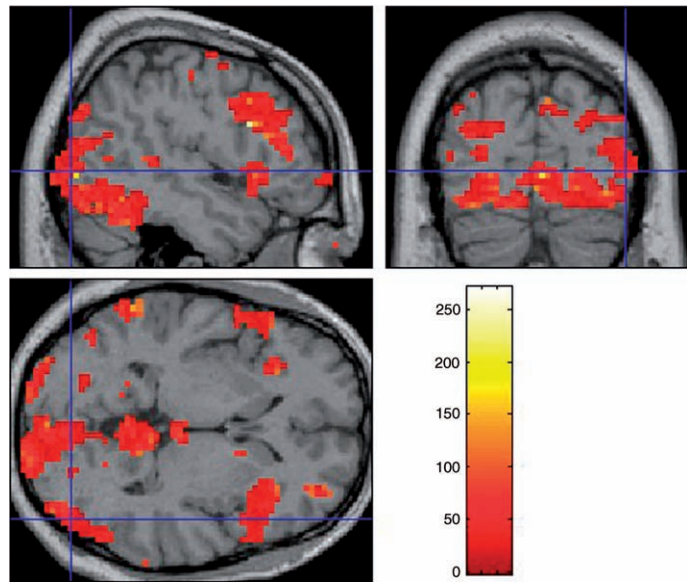


Plate 25 PPM showing above-threshold χ^2 statistics for any effect of faces.

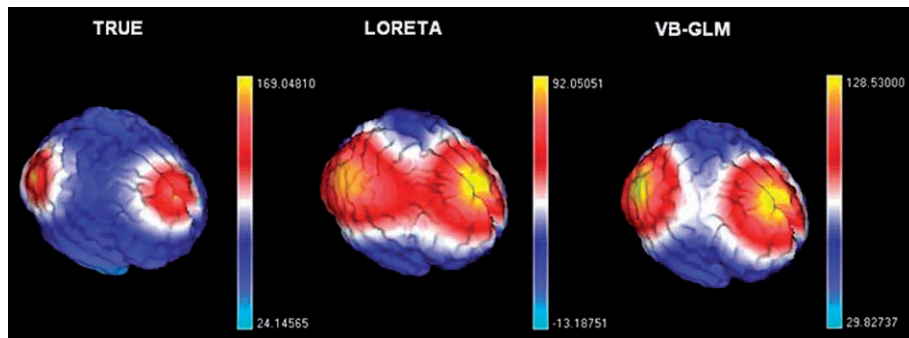


Plate 26 True and estimated source distributions at time $t = 20$ ms. Note the scaling in the figures. The VB-GLM approach is better both in terms of spatial localization and the scaling of source estimates.

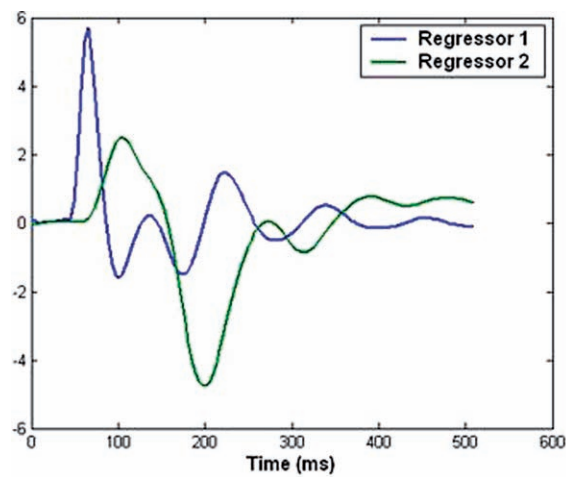


Plate 27 Two ERP components, derived from a biophysical model, used to generate simulated ERP data. These mimic an early component and a late component.

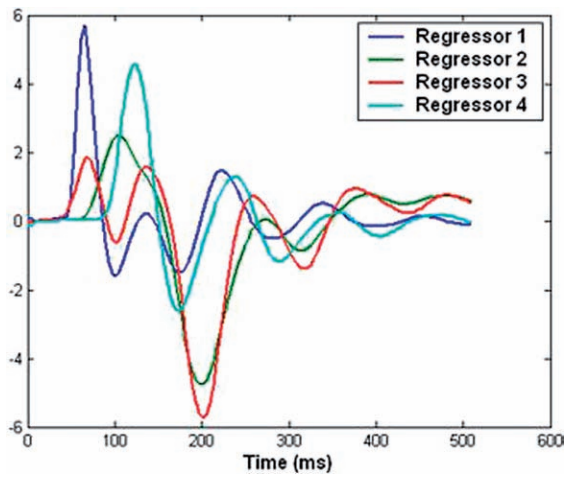


Plate 28 Four components, derived from a biophysical model, used in an over-specified ERP model.

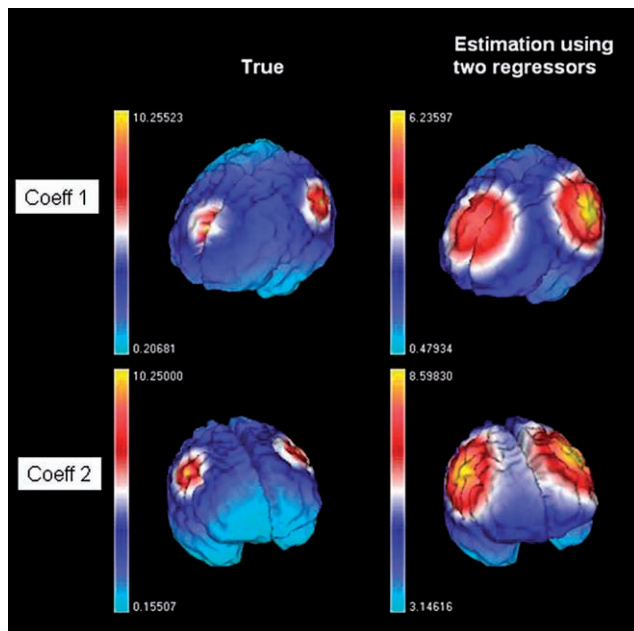


Plate 29 Regression coefficients, w_g , from ERP simulation. 'Coeff 1' and 'Coeff 2' denote the first and second entries in the regression coefficient vector w_g . True model (left) and estimates from correctly specified model (right).

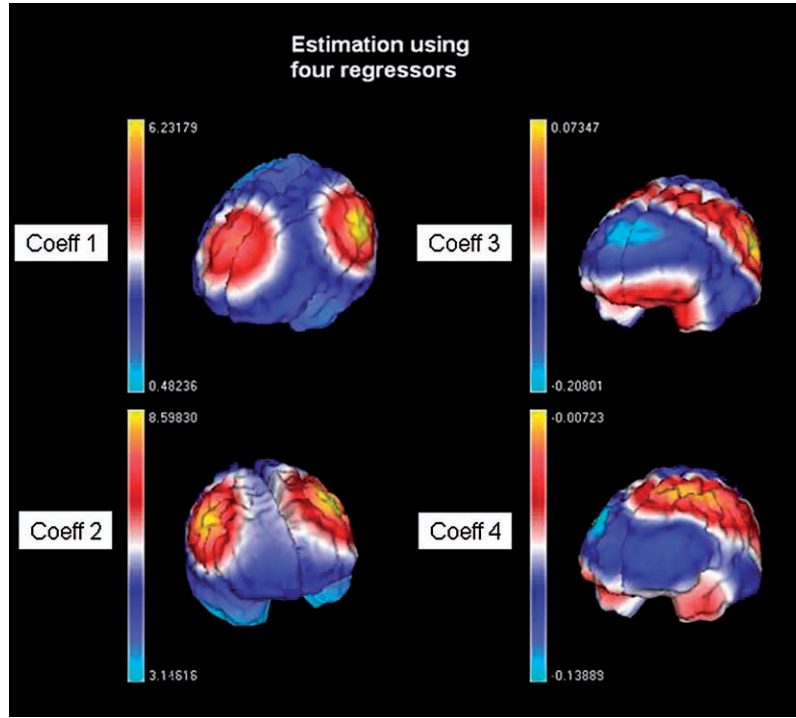


Plate 30 Estimated regression coefficients, \hat{w}_g , from over-specified model. The true coefficients are shown in Plate 29. Note the scaling of coefficients 3 and 4 (the true values are zero). Despite the high temporal correlation between regressors 2 and 3, the coefficients for regressor 3 have been correctly shrunk towards zero. This is a consequence of the spatial prior and the iterative nature of the spatio-temporal deconvolution (see Figure 26.6).

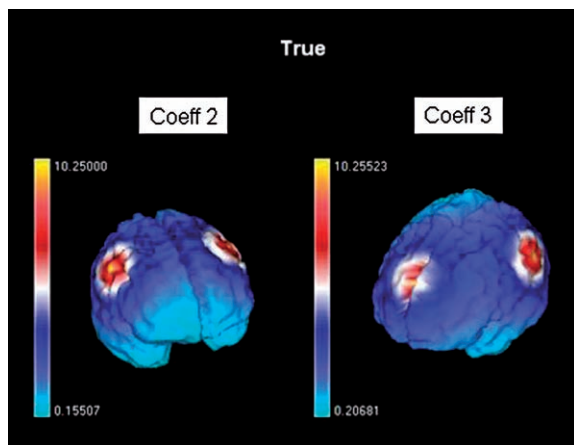


Plate 31 True regression coefficients for ERP simulation with correlated sources. This simulation used a design matrix comprising the regressors shown in Plate 28, with the first and fourth coefficients set to zero and the second and third set as shown in this figure.

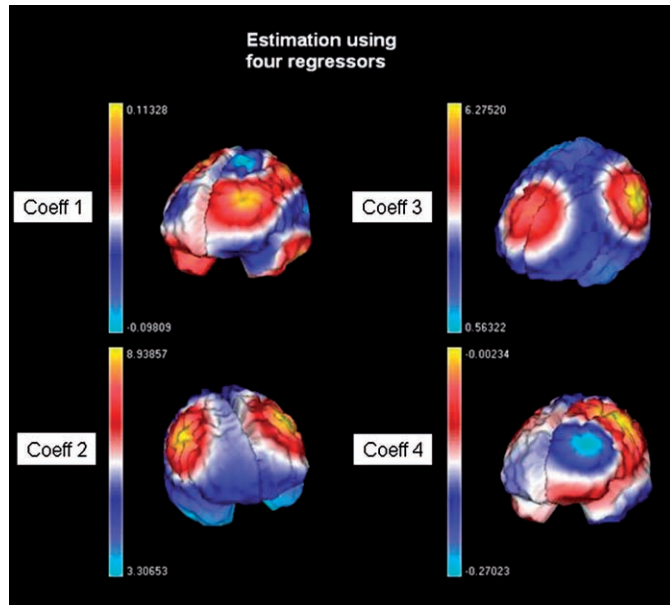


Plate 32 Estimated regression coefficients, \hat{w}_g , for ERP simulation with correlated sources. Coefficients 2 and 3 resemble the true values shown in Plate 31, whereas regressors 1 and 4 have been correctly shrunk towards zero by the spatio-temporal deconvolution algorithm.

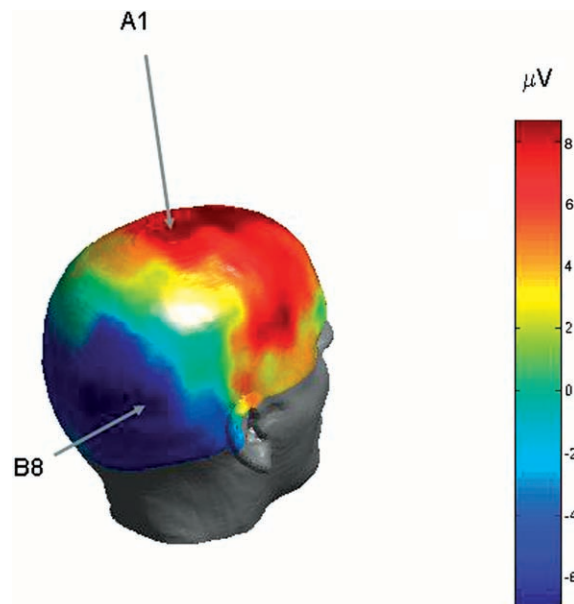


Plate 33 The figure shows differential EEG topography for faces minus scrambled faces at $t = 160$ ms poststimulus.

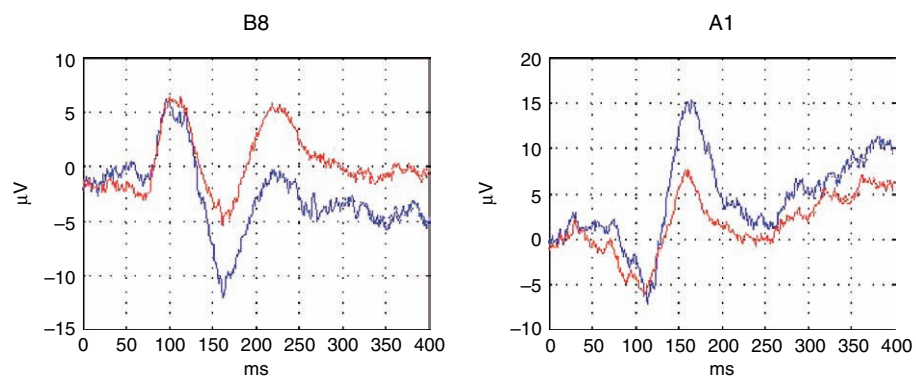


Plate 34 Sensor time courses for face data at occipito-temporal electrode B8 (left) and vertex A1 (right) for faces (blue) and scrambled faces (red).

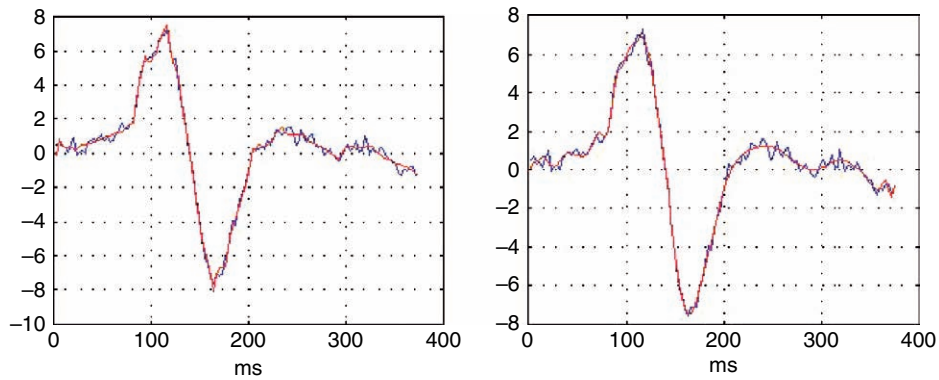


Plate 35 First eigen-time-series of downsampled ERP for unfamiliar faces (blue lines in both plots) with wavelet shrinkage approximations using Daubechies basis (left) and Battle-Lemarie basis (right).

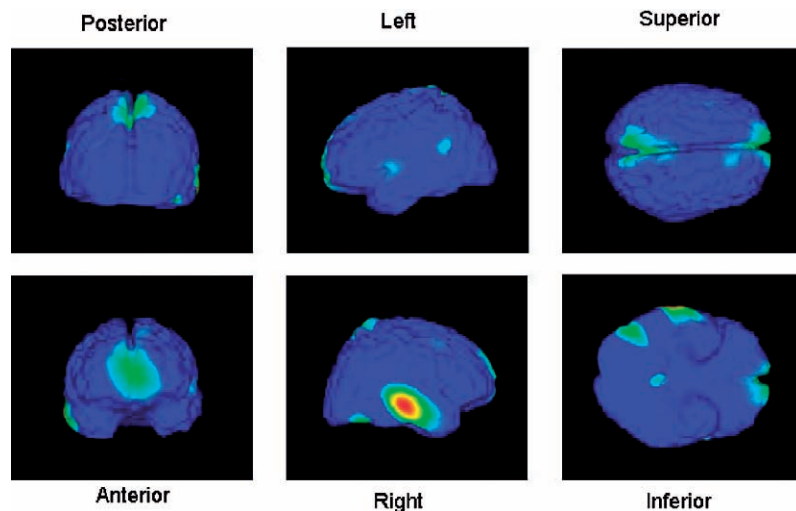


Plate 36 These images are derived from the source reconstruction of ERPs in response to faces and scrambled faces. The plots show absolute differences between faces and scrambled faces at $t = 160$ ms post-stimulus. The maps have been thresholded such that the largest difference appears in red and 50 per cent of the largest difference appears in blue.

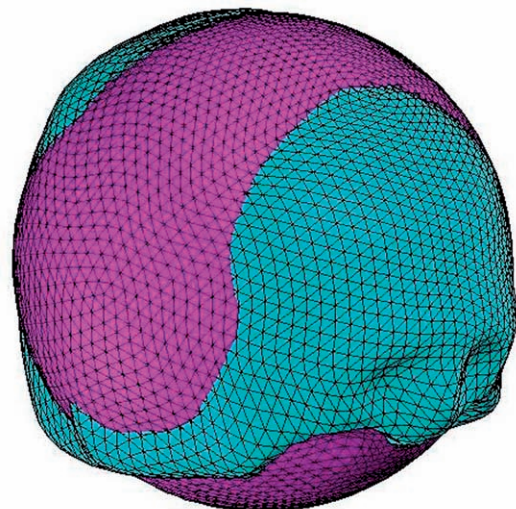


Plate 37 Best fitting sphere on a scalp surface extracted from a subject's structural MRI.

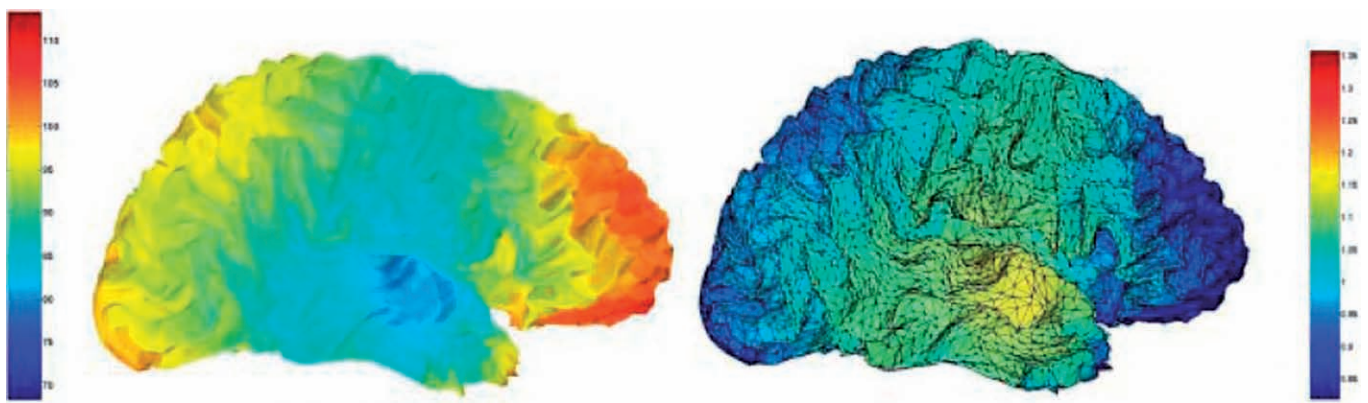


Plate 38 The left figure shows the original source location, defined by the cortical sheet. The colour scale indicates the radius of the scalp $R_{scalp}(\theta, \varphi)$ in the direction (θ, φ) of the dipole locations $(R_{sb}, \theta, \varphi)$. The right figure is the transformed source space obtained after applying Eqn. 28.60. The colour scale shows the scaling of the source radii, i.e. $R_{sphere}/R_{scalp}(\theta, \varphi)$.

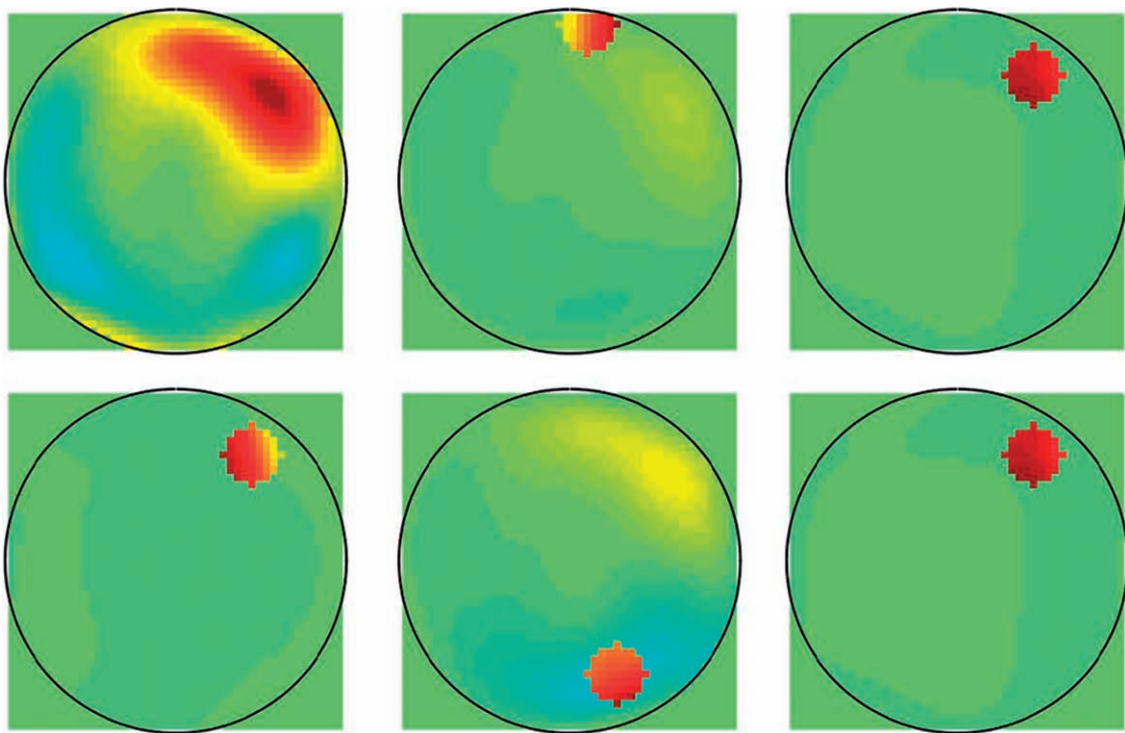


Plate 39 Reconstructed sources obtained with ReML using the example shown in Figure 29.2 (SNR = 12): no location priors (top left), with accurate location priors (bottom left), with close inaccurate location priors (top middle), with distant inaccurate location priors (bottom middle), with both accurate and close inaccurate location priors (top right) and with both accurate and distant inaccurate location priors (bottom right).

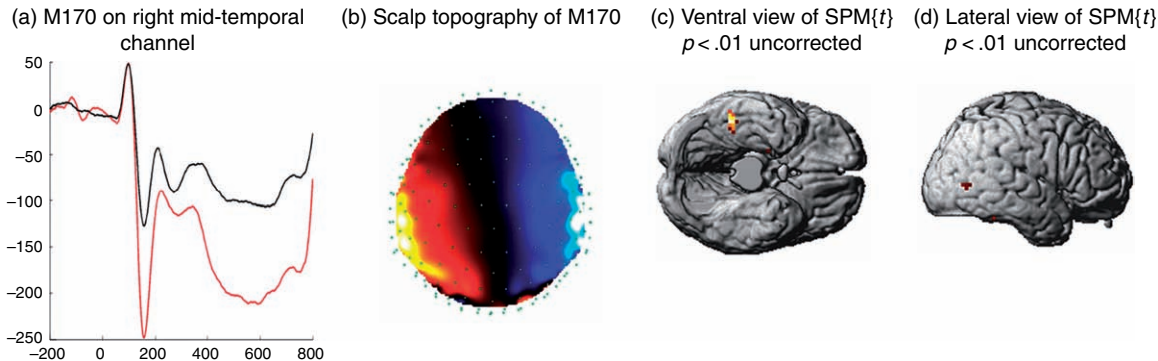


Plate 40 Multisubject analysis of face-selective response based on ReML analysis. (a) The mean M170 across participants and (b) its scalp topography. An identity matrix was used for the noise covariance in sensor space. When using only the MSP source prior, subtraction of the absolute values of the separate source reconstructions for faces versus scrambled faces revealed (c) activation of right fusiform ($+51 -39 -15$, $T(7) = 6.61$, (d) right middle temporal gyrus ($+63 -69 +3$, $T(7) = 3.48$, and right parahippocampal gyrus ($+27 -6 -18$, $T(7) = 3.32$, when thresholded at $p < 0.01$ uncorrected. MEG data from a 151-channel CTF Omega system were acquired while 9 participants made symmetry judgements to faces and scrambled faces. The MEG epochs were baseline-corrected from -100 to 0 ms, averaged over trials (approx. 70 face and 80 scrambled trials) and low-pass filtered to 20 Hz. A time-window around the peak in the global field power of the difference between the event-related field (ERF) for faces and scrambled faces that corresponded to the M170 was selected for each participant (mean window = 120–200 ms). Segmented cortical meshes of approximately 7200 dipoles oriented normal to the grey matter were created using Anatomist, and single-shell spherical forward models were constructed using Brainstorm. Multivariate source prelocalization (MSP) was used to reduce the number of dipoles to 1500. The localizations on the mesh were converted into 3D images, warped to MNI space using normalization parameters determined from participants' MRIs using SPM2, and smoothed with a 20 mm full width half maximum (FWHM) isotropic Gaussian kernel. These smoothed, normalized images were used to create an SPM of the t -statistic over participants (final smoothness approx $12 \times 12 \times 12$ mm) (c) and (d).

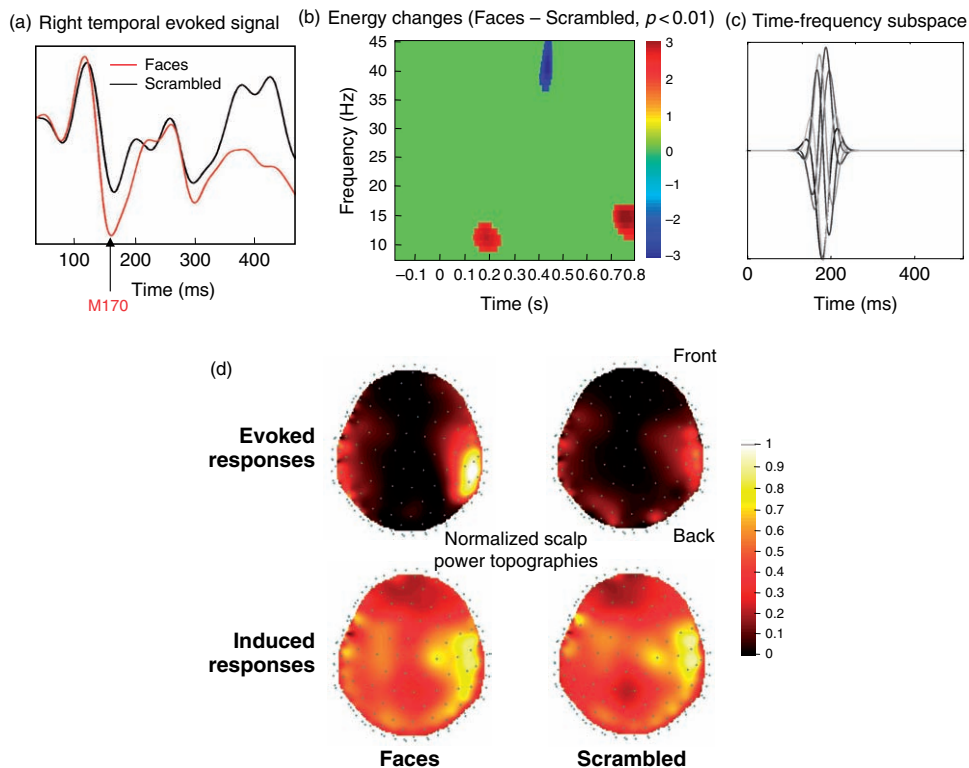


Plate 41 Real data analysis – sensor level: (a) and (b) show the differences, measured on the scalp, between faces and scrambled faces, in terms of the event-related field (ERF) from a single sensor (a), and the global energy over sensors (b) using standard time-frequency analysis and statistical parametric mapping (Kilner *et al.*, 2005). The time-frequency subspace W we tested is shown in (c) by plotting each column as a function of time. This uses the same representation as the first panel of the previous figure. This subspace tests for responses in the alpha range, around 200 ms (see corresponding time-frequency effect in (a)). The corresponding induced and evoked energy distributions over the scalp are shown in (d), for two conditions (faces and scrambled faces).

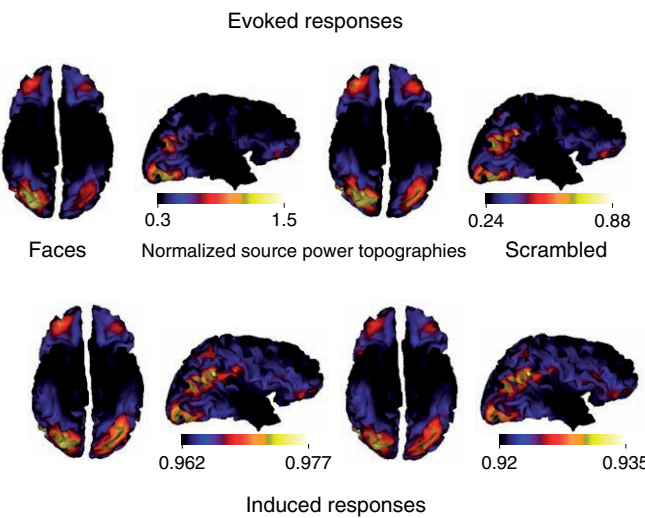


Plate 42 Real data analysis – source level: reconstructed evoked and induced responses are shown for both faces and scrambled face trials. These data correspond to conditional expectations, rendered onto a cortical surface. Note that these views of the cortical surface are from below (i.e. left is on the right). Evoked power was normalized to the maximum over cortical sources.

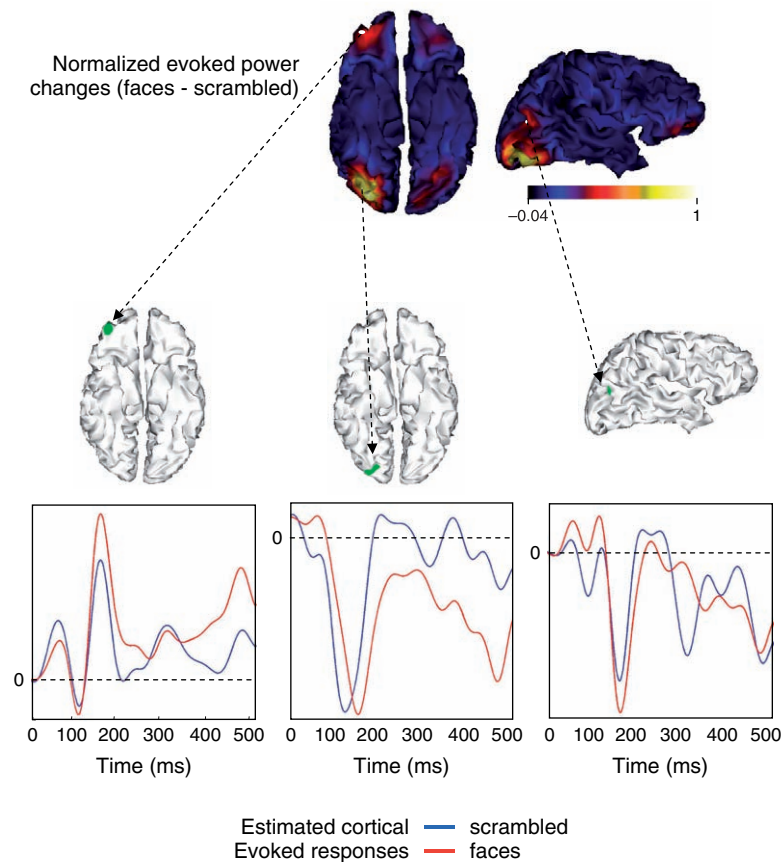


Plate 43 Real data analysis – evoked responses: the upper panels show the reconstructed evoked power changes between faces and scrambled faces. The lower panels show the reconstructed evoked responses associated with three regions where the greatest energy change was elicited.

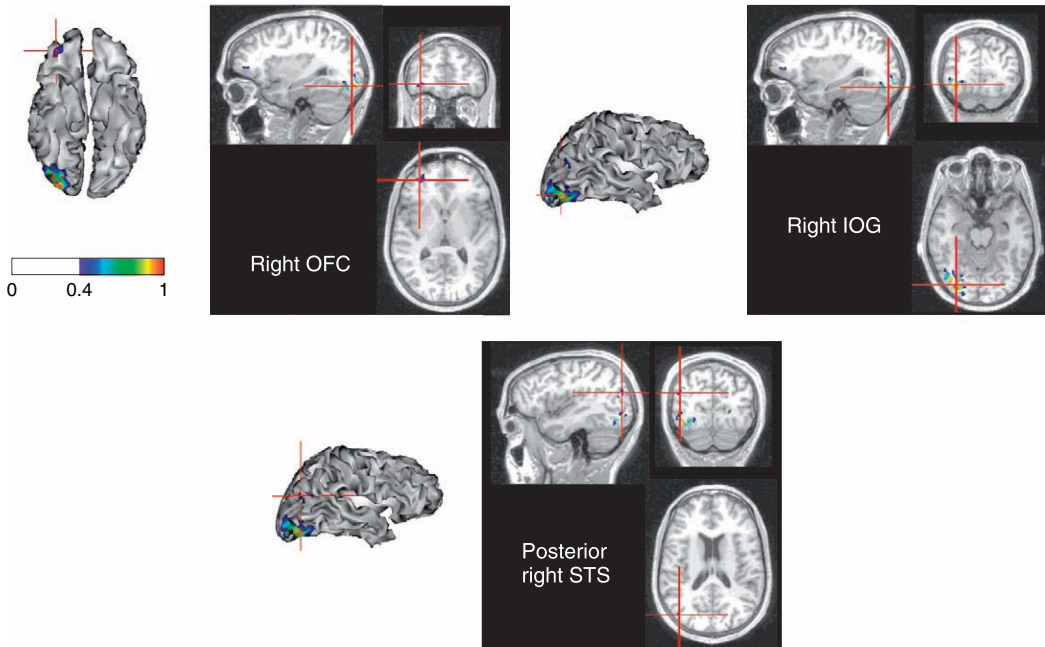


Plate 44 Visualization on the subjects' MRI: the regions identified as showing energy changes for faces versus scrambled faces in Plate 43 are shown, co-registered with a MRI scan: the right OFC (upper left panel), the right IOG (upper right panel) and the posterior right STS (lower panel). These source estimates are shown both as cortical renderings (from below) and on orthogonal sections through a structural MRI, using the radiological convention (right is left).

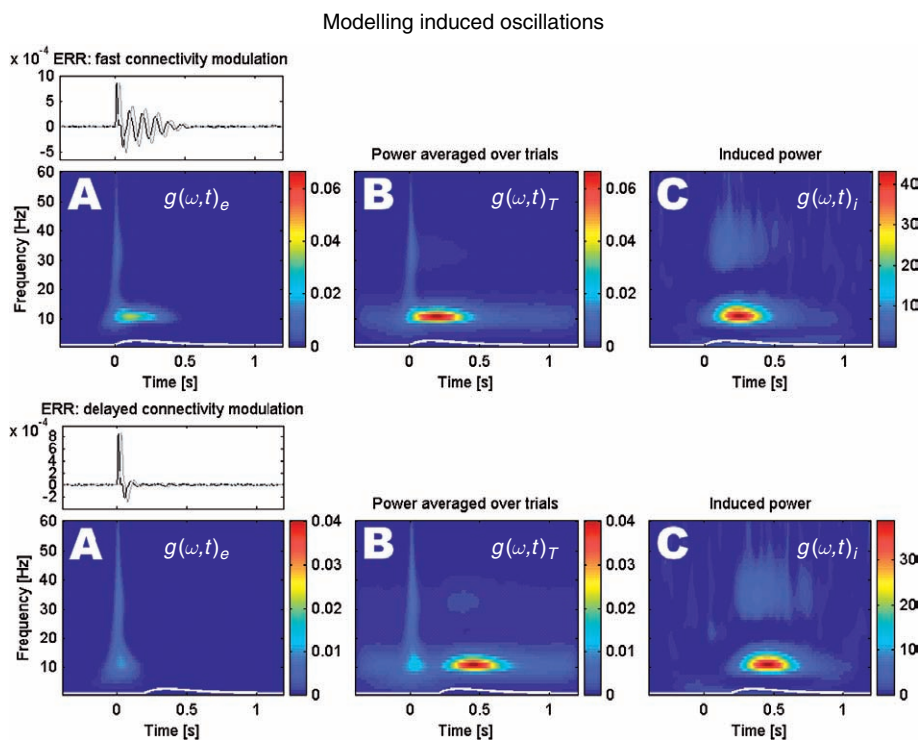


Plate 45 Upper panel: simulation of fast stimulus-related modulation of backward connectivity, using the model depicted in Figure 33.18. Black curves are the responses of area 1; grey curves correspond to area 2. Time-frequency responses are shown for area 1 only. The white line, superimposed on these spectral profiles, shows the time course of the modulatory input. (a) Evoked power, after averaging over trials, showing late oscillations that have been augmented by modulatory input. (b) Total power, averaged over trials. (c) Induced power, normalized over frequency. Lower panel: as for the upper panel, but here the modulatory effect has been delayed. The main difference is that low-frequency evoked components have disappeared because dynamic and structural perturbations are now separated in time and cannot interact. See main text for further details.

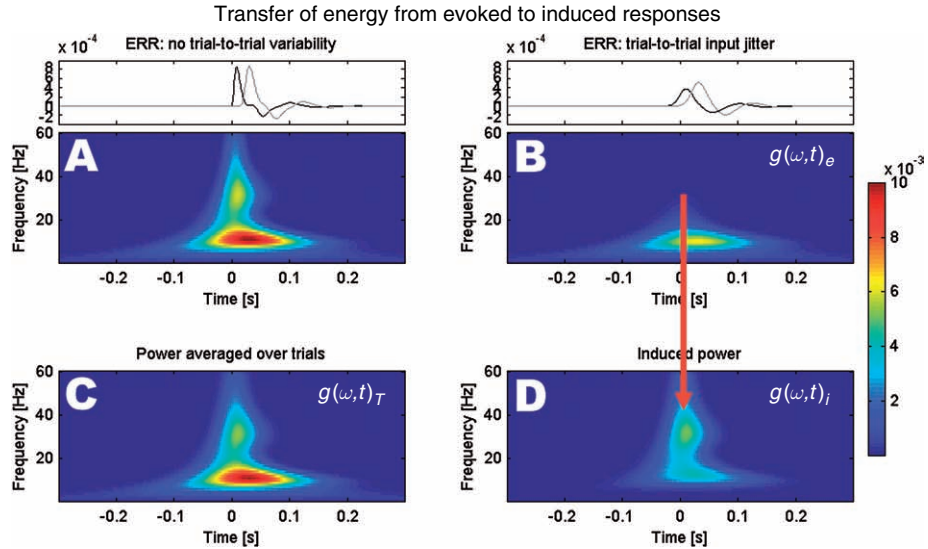


Plate 46 Simulation of trial-to-trial latency jitter (2000 trials), using the model depicted in Figure 33.18. Black curves are the responses of area 1; grey curves correspond to area 2. Time-frequency responses are shown for area 1 only. (a) Canonical response to a stimulus at time zero. (b) Evoked responses, after averaging over trials. (c) Total power, averaged over trials. (d) Induced power. As predicted, high-frequency induced oscillations emerge with latency jittering. This is due to the fact that trial-averaging removes high frequencies from the evoked power; as a result, they appear in the induced response.

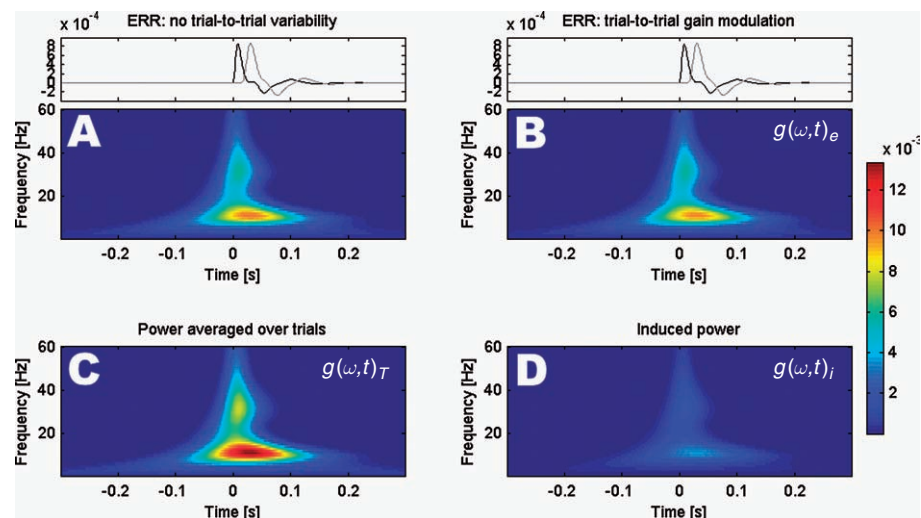


Plate 47 Simulation of gain variations over trials (2000 trials). The format is the same as in Plate 46. As predicted, although gain variation has no effect on evoked power it does affect induced power, rendering it a ‘ghost’ of the evoked power. See main text for details.

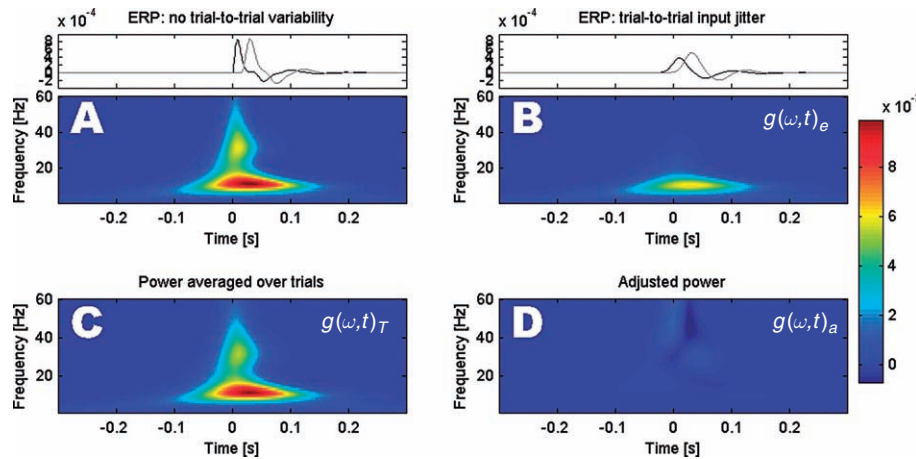


Plate 48 Adjusted power (d). The format is the same as in Plate 46. As predicted, the adjusted power is largely immune to the effects of latency variation, despite the fact that evoked responses still lose their high-frequency components.

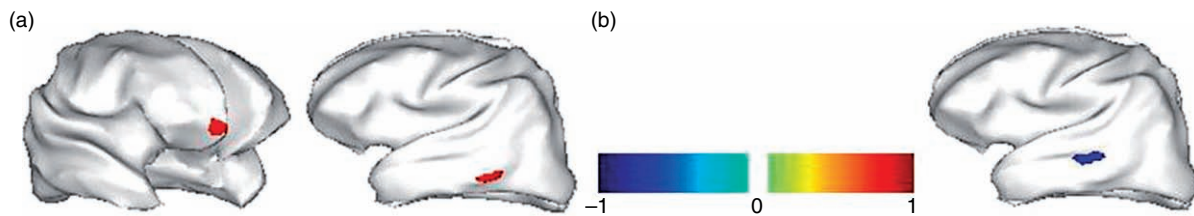


Plate 49 Inflated cortical representation of (a) two simulated source locations ('valid' prior) and (b) 'invalid' prior location.

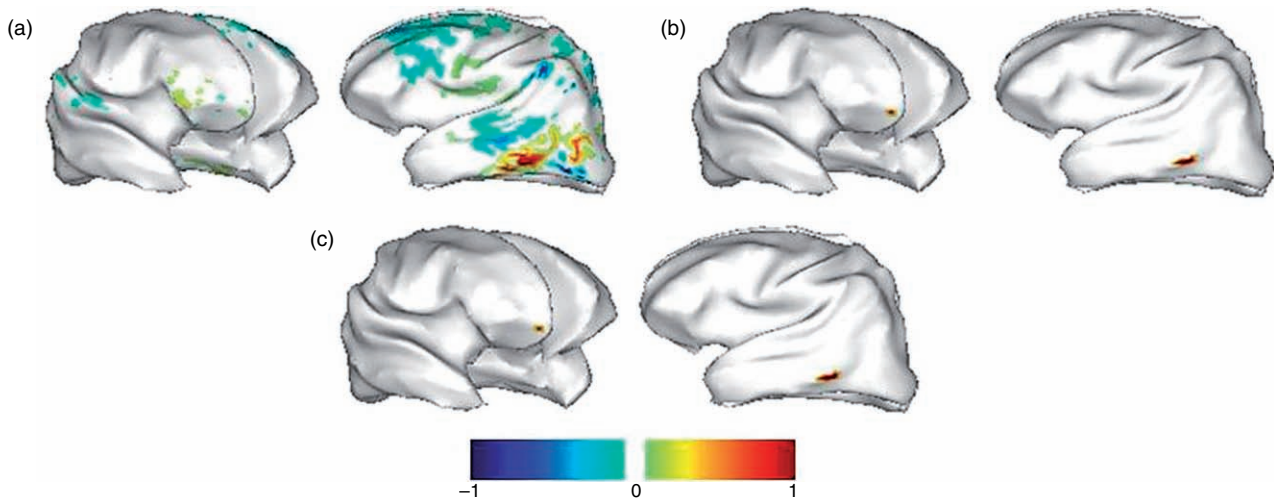


Plate 50 Inflated cortical representation of representative source reconstructions using (a) smoothness prior, (b) smoothness and valid priors and (c) smoothness, valid and invalid priors. The reconstructed values have been normalized between -1 and 1 .

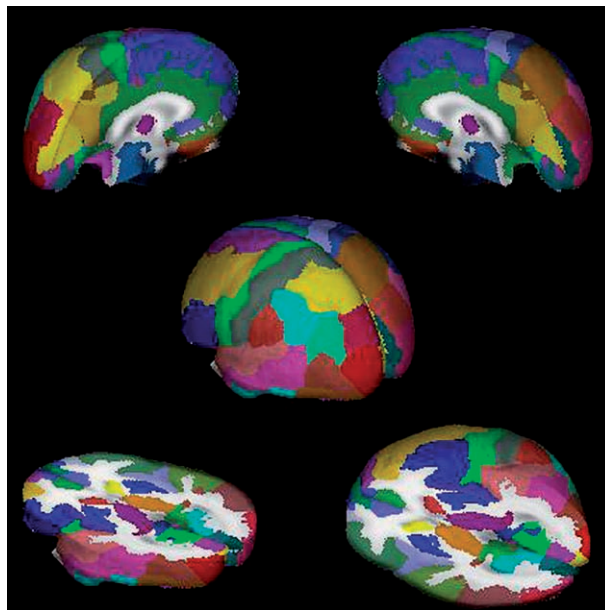


Plate 51 3D segmentation of 71 structures of the probabilistic MRI atlas developed at the Montreal Neurological Institute. As shown in the colour scale, brain areas belonging to different hemispheres were segmented separately.

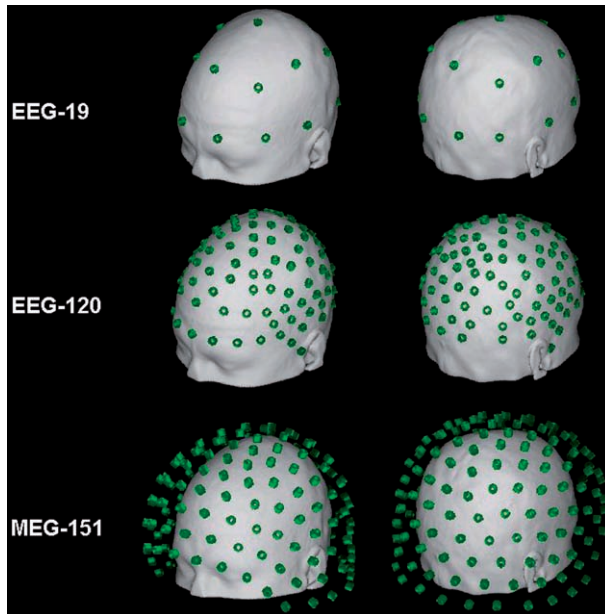


Plate 52 Different arrays of sensors used in the simulations. EEG-19 represents the 10/20 electrode system; EEG-120 is obtained by extending and refining the 10/20 system; and MEG-151 corresponds to the spatial configuration of MEG sensors in the helmet of the CTF System Inc.

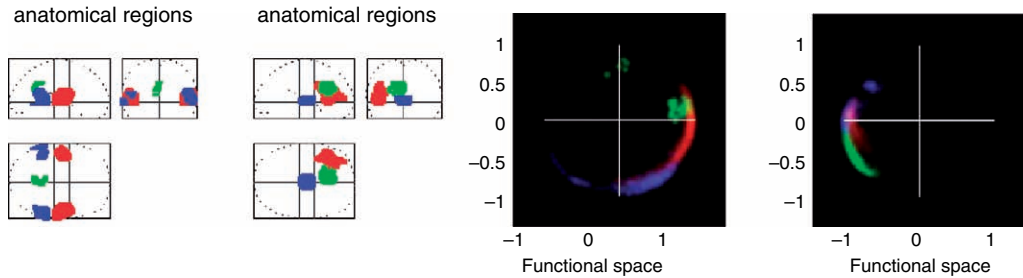


Plate 53 Classical or metric scaling analysis of the functional topography of intrinsic word generation in normal subjects. Left: anatomical regions categorized according to their colour. The designation was by reference to the atlas of Talairach and Tournoux (1988). Right: regions plotted in a functional space, following the scaling transformation. In this space the proximity relationships reflect the functional connectivity among regions. The colour of each voxel corresponds to the anatomical region it belongs to. The brightness reflects the local density of points corresponding to voxels in anatomical space. This density was estimated by binning the number of voxels in 0.02 'boxes' and smoothing with a Gaussian kernel of full width at half maximum of 3 boxes. Each colour was scaled to its maximum brightness.

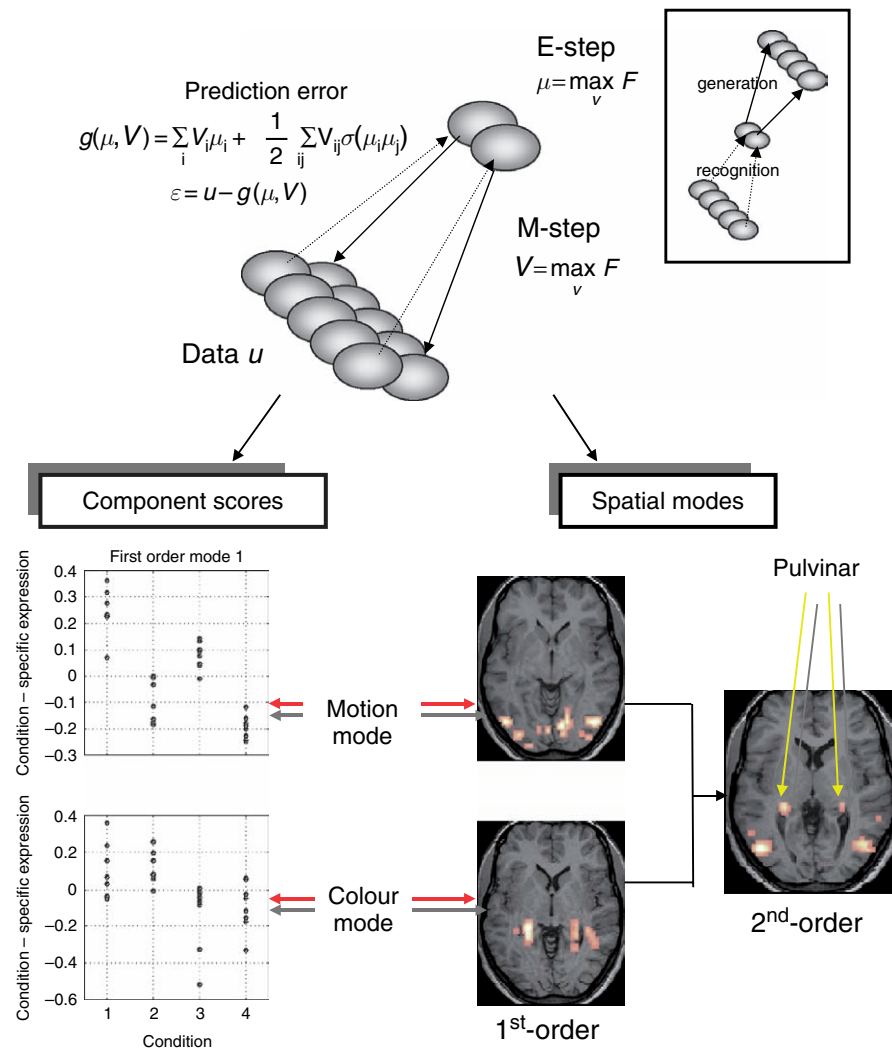


Plate 54 Upper panel: schematic of the neural net architecture used to estimate causes and modes. Feed-forward connections from the input layer to the hidden layer provide an estimate of the causes using some recognition model (the E-step). This estimate minimizes prediction error under the constraints imposed by prior assumption about the causes. The modes or parameters are updated in an M-step. The architecture is quite ubiquitous and when 'unwrapped' discloses the hidden layer as a 'bottleneck' (see insert). These bottleneck-architectures are characteristic of manifold learning algorithms, like non-linear PCA. Lower panel (left): condition-specific expression of the two first-order modes from the visual processing fMRI study. These data represent the degree to which the first principal component of epoch-related responses over the 32 photic stimulation-baseline pairs was expressed. These condition-specific responses are plotted in terms of the four conditions for the two modes. **Motion** – motion present. **Stat.** – stationary dots. **Colour** – isoluminant, chromatic contrast stimuli. **Isochr.** – isochromatic, luminance contrast stimuli. Lower panels (right): the axial slices have been selected to include the maxima of the corresponding spatial modes. In this display format, the modes have been thresholded at 1.64 of each mode's standard deviation over all voxels. The resulting excursion set has been superimposed onto a structural T1-weighted MRI image.

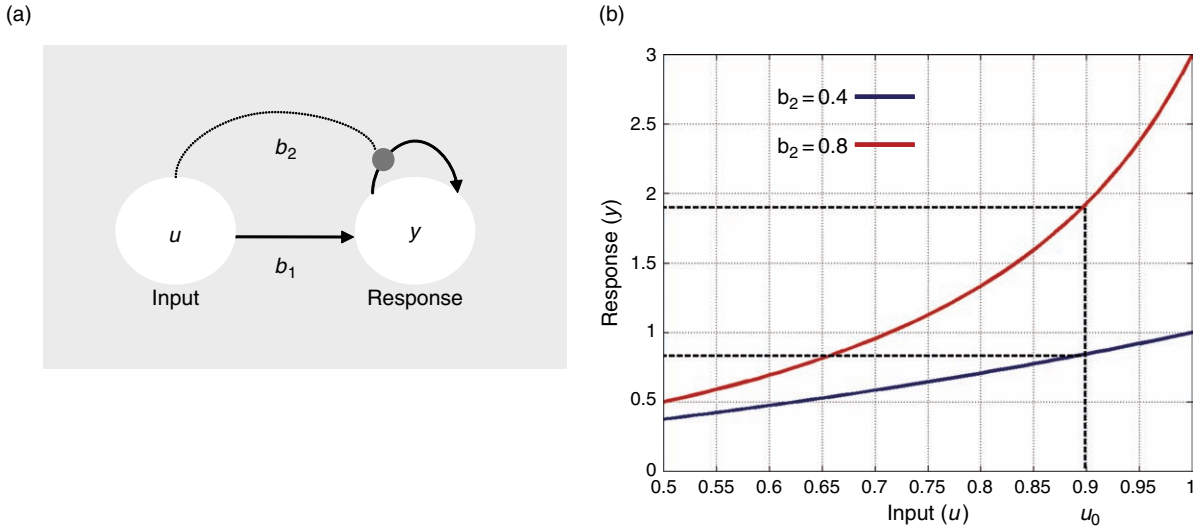


Plate 55 A simple non-linear model involving u (input) and y (response). (a) Non-linearity in the response is generated by a bilinear term uy , which models a non-additive interaction between input and intrinsic activity. The model is noise free for simplicity. The interaction term is scaled by b_2 , effectively quantifying the model's sensitivity to input at different levels of intrinsic activity. (b) Plots of input and output at different values of b_2 disclose the model's sensitivity to b_2 . At a fixed input, $u = u_0$, the response varies depending on its value.

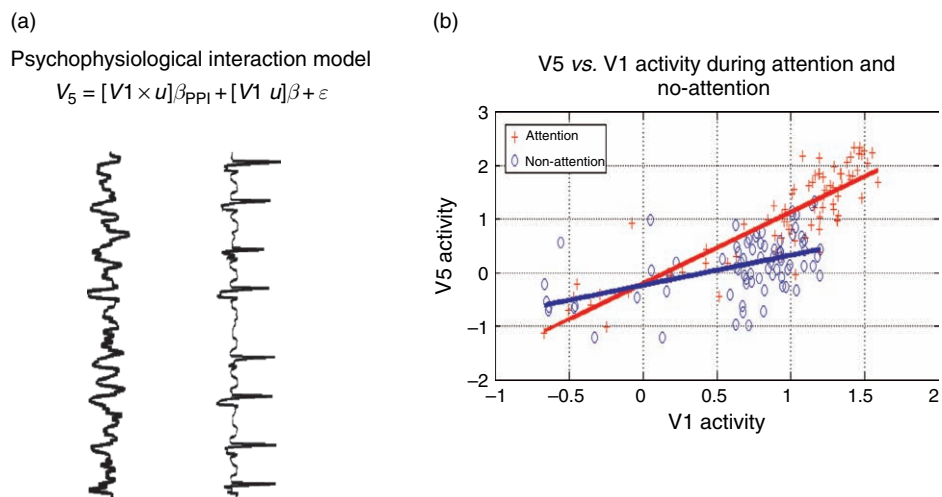


Plate 56 (a) Models for psychophysiological interaction (PPI): subjects were asked to detect changes in velocity of a radially moving stimulus or just to observe the stimulus. The velocity of the actual stimulus remained constant, so that only the attentional set changed. An analysis based on the PPI model in (a) identified a significant response in V5 that was consistent with an attentional modulation of input from V1. The PPI term is basically an interaction between attentional set, u , and V1 activity as measured with fMRI. (b) The change in sensitivity of V5 to V1 input, depending on attentional set. This is a simple comparative regression analysis, after partitioning the data according to the level of the attention factor.

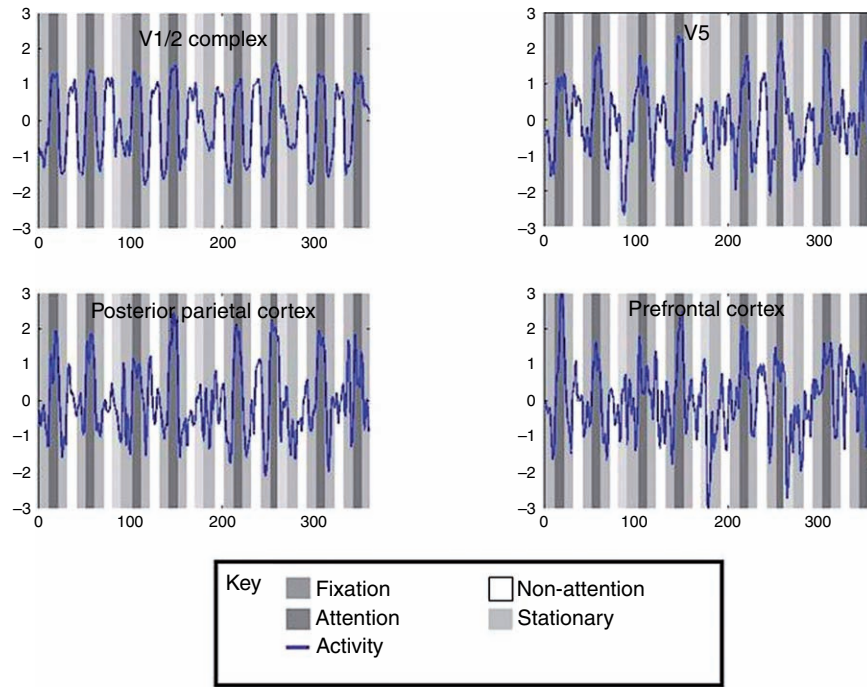


Plate 57 These are the time-series of regions V1/2 complex, V5, PPC and PFC from subject 1, in the right hemisphere. All plots have the same axes of activity (adjusted to zero mean and unit variance) versus scan number (360 in total). The experiment consisted of four conditions in four blocks of 90 scans. Periods of ‘attention’ and ‘non-attention’ were separated by a ‘fixation’ interval where the screen was dark and the subject fixated on a central cross. Each block ended with a ‘stationary’ condition where the screen contained a freeze frame of the previously moving dots. Epochs of each task are indicated by the background greyscale (see key) of each series. Visually evoked activity is dominant in the lower regions of the V1/2 complex, whereas attentional set becomes the prevalent influence in higher PPC and PFC regions.

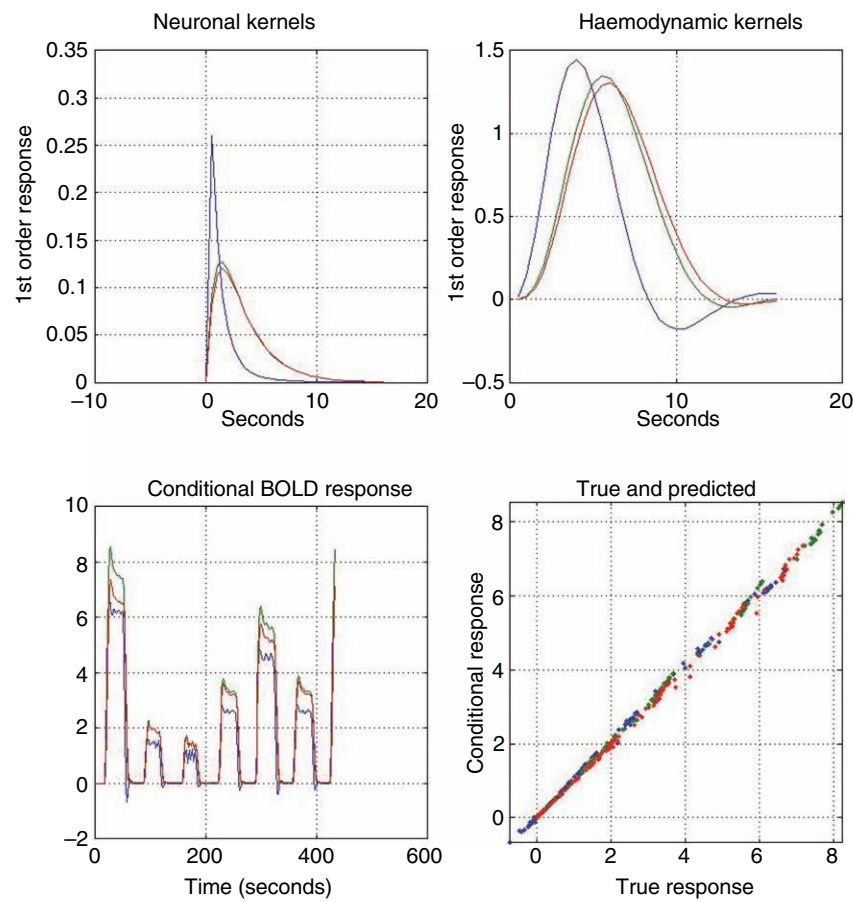


Plate 58 These results are based upon the conditional or MAP estimates of Figure 41.7. The upper panels show the implied first-order kernels for neuronal responses (upper-left) and equivalent haemodynamic responses (upper-right) as a function of peristimulus time for each of the three regions. The lower panels show the predicted response based upon the MAP estimators and a comparison of this response to the true response. The agreement is self-evident.

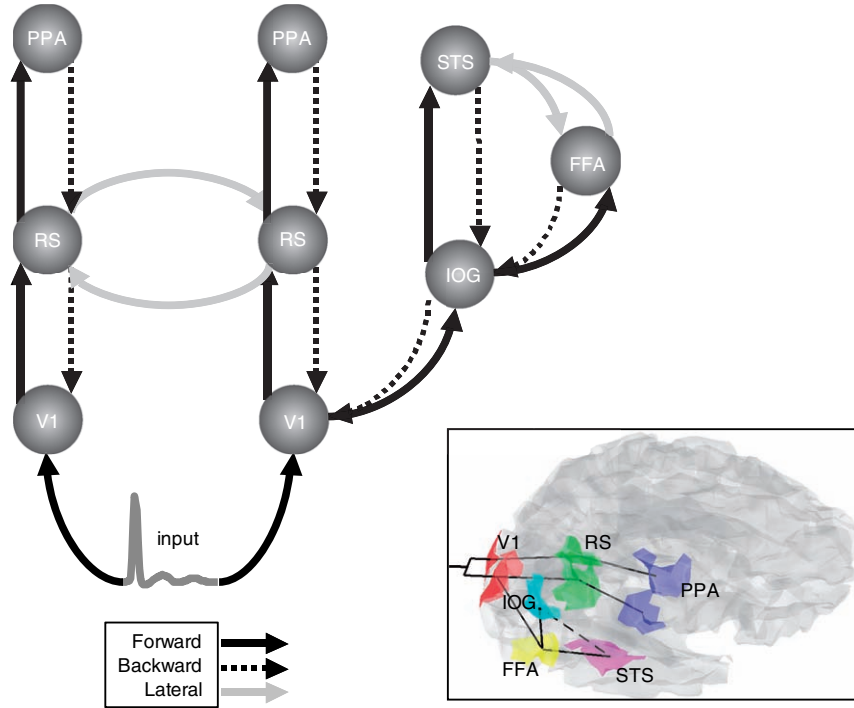


Plate 59 Model definition for the category-selectivity paradigm: the sources comprising the DCM are connected with forward (solid), backward (broken) or lateral (grey) connections as shown. V1: primary visual cortex, RS: retrosplenial cortex, PPA: parahippocampal place area, IOG: inferior occipital gyrus, STS: superior temporal sulcus, FFA: fusiform face area (left is on the left). Insert: transparent views of the subject's cortical mesh from the top-right, showing the sources that defined the lead-field for the DCM: a bilateral extrinsic input acts on the primary visual cortex (red). Two pathways are considered: (i) bilaterally from occipital regions to the parahippocampal place area (blue) through the retrosplenial cortex (green, laterally interconnected); (ii) in the right hemisphere, from primary visual areas to inferior occipital gyrus (yellow) which projects to the superior temporal sulcus (cyan) and the lateral fusiform gyrus (magenta). The superior temporal sulcus and lateral fusiform gyrus are laterally connected.

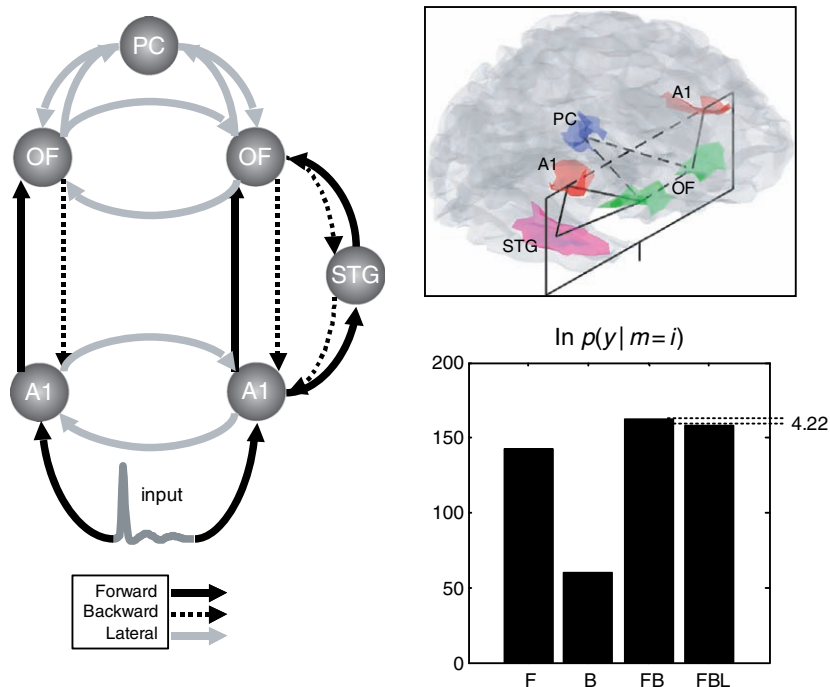
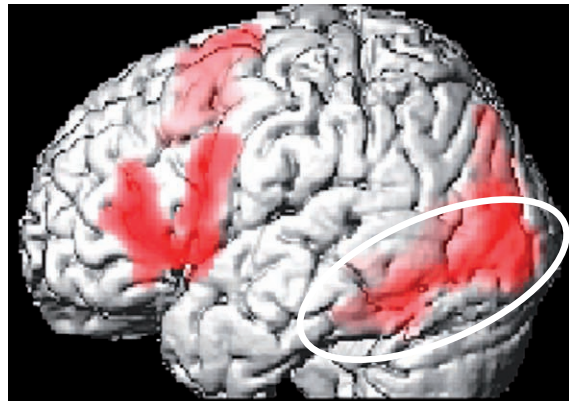


Plate 60 DCM specification for the auditory oddball paradigm: Left: graph depicting the sources and connections of the DCM using the same format as Plate 59: A1: primary auditory cortex, OF: orbitofrontal cortex, PC: posterior cingulate cortex, STG: superior temporal gyrus. Insert: localized sources corresponding to the lead fields that entered the DCM: a bilateral extrinsic input acts on primary auditory cortex (red) which project to orbitofrontal regions (green). In the right hemisphere, an indirect pathway was specified, via a relay in the superior temporal gyrus (magenta). At the highest level in the hierarchy, orbitofrontal and left posterior cingulate (blue) cortices were assumed to be laterally and reciprocally connected. Lower right: results of the Bayesian model selection among DCMs allowing for learning-related changes in forward F, backward B, forward and backward FB and all connections FBL. The graph shows the Laplace approximation to the log-evidence and demonstrates that the FB model supervenes. The log-evidence is expressed relative to a DCM in which no connections were allowed to change.



Letter decisions > Spatial decisions

Plate 61 Results from an SPM analysis of the fMRI data from Stephan *et al.* (2003). Comparing letter decisions to visuo-spatial decisions about identical stimuli showed strongly left-lateralized responses, including classical language areas in the left inferior frontal gyrus and visual areas in the left ventral visual stream (white ellipse), e.g. in the fusiform gyrus, middle occipital gyrus and lingual gyrus. Results are shown at $p < 0.05$, corrected at the cluster level for multiple comparisons across the whole brain. Adapted, with permission, from Figure 1 in Stephan *et al.*, 2003.

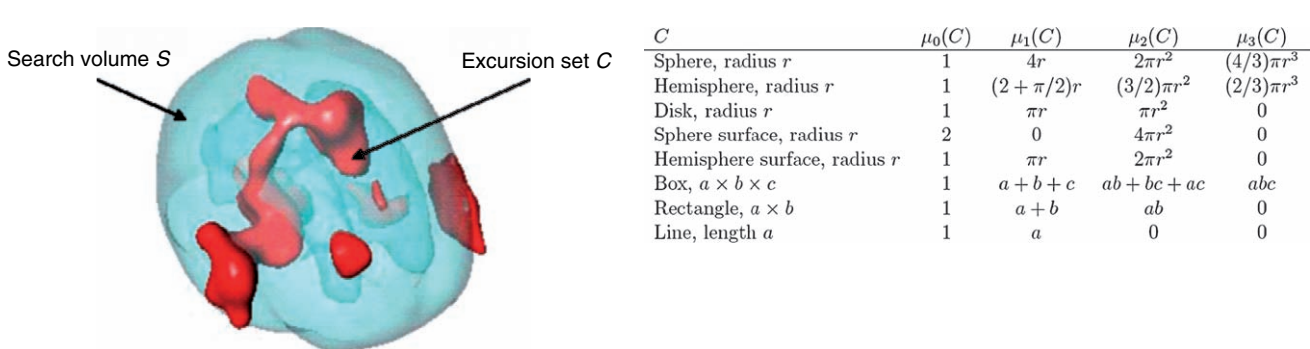


Plate 62 Left: picture of a search volume $S \subset \mathbb{R}^D$ and its excursion set $C = \{t \in S : X(t) > x\}$, defined by a height threshold x . Right: Minkowski functionals for some common search volumes. After statistical flattening (i.e. with unit roughness) these correspond to the resel counts.